University of Padova

Department of Industrial Engineering DII
Master's Degree Course in Aerospace Engineering

Space Tether Deployer Prototype Design and Laboratory Testing

Supervisor:	Prof. Enrico Lorenzini
Co-supervisor:	Dott. Lorenzo Olivieri
Co-supervisor:	Dott. Andrea Valmorbida

Author: Davide Vertuani
mat. 1197630

December 3rd, 2020 - Academic year 2019/2020

```
import acknowledge
peopleToAcknowledge = getAcknowledgmentList()
for person in peopleToAcknowledge:
    print("%s, thank you so much!" %(person))
```

Abstract

This thesis deals with the design and development of a space tether deployer prototype and its first tests in a controlled laboratory environment. The design of the mock-up aims at faithfully reproducing - as far as a testbed with limited resources can reasonably do - the Deorbiting Kit under development by the E.T.Pack consortium; this European project is targeting 2022 as the first deployment test of its commercial and spacecraft-agnostic independent module, with the goal of helping reducing the orbital debris pollution by proposing an easier and cheaper deorbiting solution. With this goal, a testbed has been conceived and designed. It exploits a testing facility for reduced friction simulations (SPARTANS, developed at the University of Padova) and is the result of a conjunct effort of two thesis works. In this document the selection and sizing of two motors for tape deployment and braking are described, as well as the control and data handling subsystem. Two stepper motors have been employed to drive the tape reel, precisely controlling the deployment rate to match the expected and precomputed profile, as this is a mission critical requirement. Control and telemetry transmission happen on a wireless ad-hoc subnet and take advantage of the lightweight and versatile MQTT protocol, allowing expandability of the control network to a virtually unlimited number of machines and similarly utilization of numerous sensors and WiFi-enabled microcontrollers. The control interface is realized in MATLAB, thus obtaining a seamless data acquisition and processing pipeline. Qualification and assembly tests have been conducted prior the experimental campaign, which has seen the execution of three main characterization and functional tests. Further testing and development is planned for this mock-up, promising to enable valuable experimentation for space tethered applications.

Sommario

Questo lavoro di tesi affronta il design e lo sviluppo di un prototipo di svolgitore per tether spaziali ed i suoi primi test in ambiente controllato di laboratorio. Il design del modello rappresentativo mira a riprodurre fedelmente - limitatamente a quanto permesso da un banco di prova dalle ristrette risorse - il *Deorbiting Kit* in sviluppo dal consorzio di E.T.Pack; questo progetto europeo mira al 2022 come anno del primo test di utilizzo per il suo modulo, indipendente dalla tipologia di satellite, con l'obiettivo di aiutare a ridurre l'inquinamento dei detriti orbitali proponendo una soluzione di deorbitazione più semplice e economica. Con questo scopo, è stato concepito e realizzato un banco di prova. Esso sfrutta una struttura per simulazioni ad attrito ridotto (SPARTANS, sviluppato all'Università di Padova) ed è il risultato dello sforzo congiunto di due lavori di tesi. Nel presente documento sono descritti la selezione ed il dimensionamento di due motori per lo sviluppo e la frenata del nastro, assieme ai sottosistemi di controllo e gestione dei dati. Due motori stepper sono stati utilizzati per azionare la bobina del nastro, controllando con precisione la velocità di svolgimento, essendo questa critica per la missione. Il controllo e la trasmissione della telemetria avvengono tramite una sottorete wireless creata appositamente, e traggono vantaggio del leggero protocollo MQTT, permettendo così l'espansione della rete di controllo ad un numero virtualmente illimitato di macchine, e similmente l'utilizzo di numerosi sensori e microcontrollori wireless. L'interfaccia di controllo è stata realizzata in MATLAB, ottenendo in tal modo un fluido processo di acquisizione e elaborazione dei dati. Test di qualifica e di sistema sono stati svolti prima della compagna sperimentale, che ha visto l'esecuzione di tre prinicipali test di caratterizzazione e funzionali. Ulteriori sviluppi sono previsti per questo modello, che promette di rendere possibile altri utili esperimenti per applicazioni di tether spaziali.

Contents

List of Figures

List of Tables

Acronyms

ADC Analog to Digital Converter.
ASI Agenzia Spaziale Italiana (Italian Space Agency).

BLDC BrushLess DC.

CAD Computer-Aided Design.
CNES Centre National d'Études Spatiales (French Space Agency).

DK Deorbit Kit.
DLR Deutsches Zentrum für Luft- und Raumfahrt (German Space Agency).
DoF Degrees of Freedom.

E.T.Pack Electrodynamic Tether Technology for Passive Consumable-less Deorbit Kit.
EDT Electro Dynamic Tethers.
ESA European Space Agency.

FDM Fused Deposition Modeling.

GEO Geostationary Earth Orbit.
GPIO General Purpose Input/Output.

HEO High Earth Orbit.

IADC Inter-Agency Space Debris Coordination Committee.

LEO Low Earth Orbit.

MC Motion Capture.

PARCAE Pulleys, Actuator, and Roll Compression Assembly for E.T.Pack.
PLA Polylactic acid.
PWM Pulse Width Modulation.

SLS Selective Laser Sintering.

SPARTANS SPAcecRraft Testbed for Autonomous proximity operatioNs experimentS.

UKSA UK Space Angency.
UN United Nations.

Chapter 1

Introduction

Orbital debris are becoming a threat to future space utilization and operability; space agencies and spacecrafts operators are leading the path to more responsible disposal procedures for spent payloads, suggesting to deorbit decommissioned objects in less than 25 years from the end of service and generally to minimize the release of mission-related objects. Electrodynamic tethers are promising a cheap and effective approach to the problem; in this scenario, the European project E.T.Pack is leading the path to an accessible, spacecraft-independent Deorbiting Kit.

1.1 The space debris problem

In the last few decades, starting from the first orbital flights in the 1960s, the space industry has witnessed a steady and rapid growth, with more and more countries and companies taking their place into this profitable market and exploiting the several opportunities it has to offer. Nowadays, our society makes use of orbital technologies for a variety of applications, including telecommunications, global navigation, weather forecast, Earth observation, pollution assessment and many more, making robotic spacecrafts an essential tool to sustain the lifestyle of the modern civilization.

To date, more than 5540 active spacecraft are on orbit, together with an approximate population of 14 790 inactive bodies over 10 cm of diameter [3], such as decommissioned spacecrafts, rocket upper stages, mission related objects and generic collisional debris, amounting at around 20 500actively tracked items (see Figure 1.1). In addition, around $1.29 \cdot 10^{-8}$ non trackable, small scaled debris with a diameter between 1 mm and 10 cm are estimated to be orbiting Earth, predominantly in the LEO and HEO zones as reported in Figure 1.2 [2]. For this kind of bodies, mathematical models are available (ESA MASTER [4], NASA LEGEND [5]).

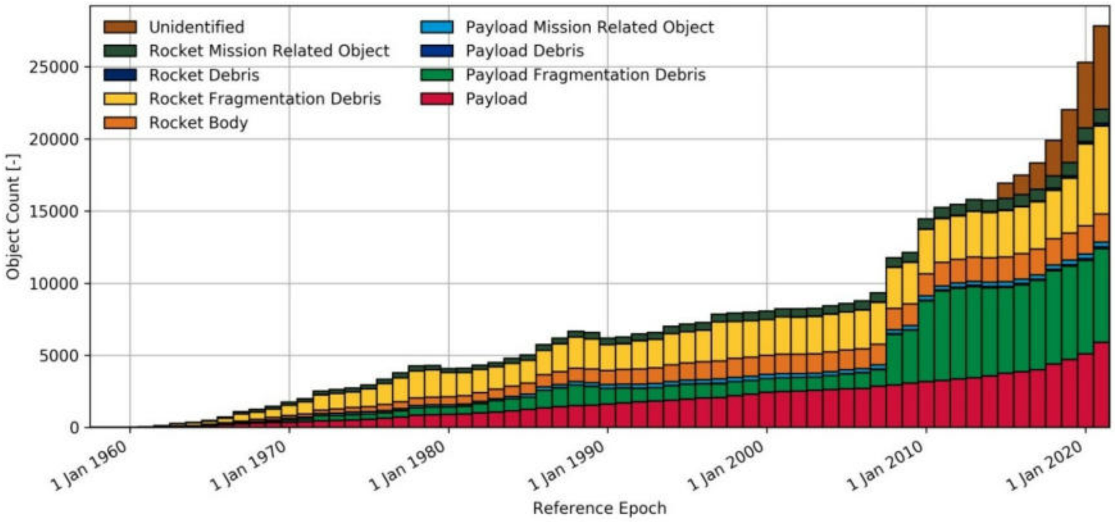

Figure 1.1: Orbital objects count by category. Active spacecrafts indicated in red.
Source: ESA Space Environment Report [2]

These statistics are destined to drastically increase in the next future: new approaches to internet broadcasting have been proposed by several corporations, which are planning to establish large LEO constellations capable of low latency, high speed intercontinental links. As an example, *SpaceX'* plans for its large constellation *Starlink* are to bring to orbit about 12 000 satellites by 2022, with more than 700 already launched [6], whereas *Blue Origin* already asked band allocations for their upcoming 3236 satellites [7]. This would likely cause the current orbital population to more than double in a matter of years, primarily involving the already crowded LEO orbits.

While the increase of operational spacecrafts is not yet a problem on its own[1], the management of decommissioned payloads is, on the contrary, at the center of the debate. Moving objects or varying their orbit in space is always an expensive operation, especially if it relies on valuable on-board consumables: propulsion propellant mass is used to extend the payload life and has been paid for at liftoff, so making use of it for non-profitable operations does not make financial sense; as a consequence, the vast majority of spacecrafts operators tends to abandon spent payloads in their orbits instead of removing - deorbiting - them, contributing to feed the "debris belt". Depending on the orbit and on the ballistic coefficient, defined as mass over cross-sectional area,

$$\beta = \frac{m}{c_D A}$$

---

[1] The first avoidance maneuver between two active spacecrafts was performed by ESA's Aeolus to avoid one of SpaceX' Starlink satellites, on September 2nd, 2019

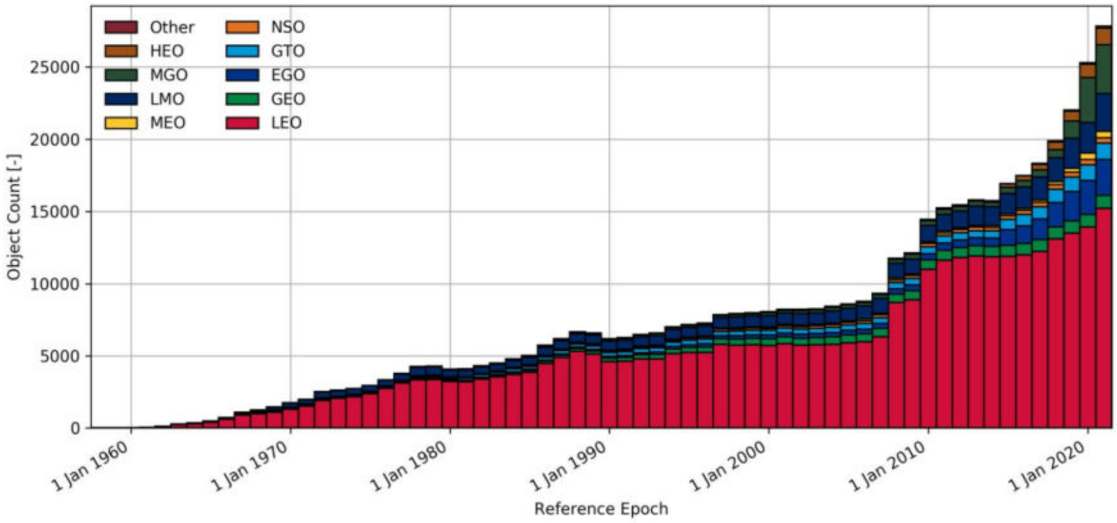

Figure 1.2: Orbital objects count by orbit. Note the LEO predominancy.
Source: ESA Space Environment Report [2]

these objects will remain in situ for time periods ranging from some years (1 year in LEO, $h = 200km$, $\beta = 10kg/m^2$, or 100 years in LEO, $h = 200km$, $\beta = 1.000kg/m^2$) to 10^6 years (GEO, $h = 36.000km$) [2] [8].

Nourishing the debris belt will eventually harm our ability to safely and efficiently operate space missions. Even if it is still an unlikely hazard, keeping on leaving ungovernable bodies in space could lead to what is by now widely known as the *Kessler Syndrome*, i.e. an exponential increase of debris due to a collisional cascade, posing a significant threat to future space operability and spacecrafts' lifespan [9,10]. As stated by Kessler et al. [9],

> *In order to prevent this growth, we are at a point where we must obtain near 100% compliance with guidelines established over 10 years ago and, in addition, we must retrieve a number of objects that are already in orbit.*

This is why the space community urges to adopt effective countermeasures able to mitigate the problem and assure safe access to space to future generations.

---

[2] Spacecrafts in GEO are not deorbited at end of life, and are cited here only for example purposes.

1.2 Guidelines and normative

As of now, no international regulations have been defined to control spacecrafts decommissioning and debris removal. In 2010, the United Nations Organization Committee on the Peaceful Uses of Outer Space issued the pace Debris Mitigation Guidelines [11], suggesting that member States should, according to their own sensibility, adhere to the suggested post-mission disposal procedures.
As reported by the document,

> *Member States and international organizations should voluntarily take measures, through national mechanisms or through their own applicable mechanisms, to ensure that these guidelines are implemented, to the greatest extent feasible, through space debris mitigation practices and procedures.*

The aforementioned guidelines present a "set of mitigation guidelines", of which the summaries are cited below:

- Limit the debris released during normal operations.
- Minimize the potential for break-ups during operational phases.
- Limit the probability of accidental collision in orbit.
- Avoid intentional destruction and other harmful activities.
- Minimize potential for post-mission break-ups resulting from stored energy.
- Limit the long-term presence of spacecraft and launch vehicle orbital stages in the low-Earth orbit (LEO) region after the end of their mission.
- Limit the long-term interference of spacecraft and launch vehicle orbital stages with the geosynchronous Earth orbit (GEO) region after the end of their mission.

Namely, no precise indication about the maximum allowed permanence in orbit of decommissioned spacecrafts is given, no fine or penalty are considered, no real law article is issued. Therefore Space still remains a partially unregulated environment; it is fair to assume that the guidelines will be followed either by those who do not operate purely to realize a financial return or if the cost sustained to safely deorbit is negligible with respect to the mission profit.

On the other hand, space agencies were already independently adopting more technical common codes of conduct; the *European Code of Conduct for Space Debris Mitigation* [12], on which the UN Guidelines are based on, signed by ASI, UKSA, CNES, DLR and ESA in 2006, clearly states:

> *The operator of a space system should perform disposal maneuvers at the end of the operational phase to limit the permanent or periodic presence of its space system in the protected regions to a maximum of 25 years. This can be achieved, in decreasing order of preference:*
>
> – *either by performing a direct re-entry of the space system;*
> – *or by limiting the orbital lifetime of the space system to less than 25 years after its operational phase;*
> – *or by transferring the space system to a disposal orbit.*

As a further step, the guidelines are now found unified by the *IADC Space Debris Mitigation Guidelines* [13] adopted and signed in 2007 by the thirteen IADC member agencies.

1.3 Mitigation strategies

As previously stated, the currently suggested approach to the problem of orbital debris consists of either removing the object from its orbital shell and deorbiting it in less than 25 years, or transferring it to a designed disposal orbit where it will not interfere with future missions. Since the debris problem is mainly seen in LEO sectors, from where a reentry is usually possible, we will hereby consider only the common deorbiting strategies.
Currently, three deorbiting strategies are widely adopted:

- **Uncontrolled deorbiting:**
  or natural decay. Consisting in maneuvering into an orbit in which the drag from the residual atmosphere will cause the spacecraft to reenter in less than 25 years.
- **Passive controlled deorbiting:**
  requires no or minimal power input; usually a little amount of power is needed to deploy the reentry system. This approach makes use of solar sails, drag sails or inflatable balloons, or electrodynamic tethers.
- **Active controlled deorbiting:**
  require power to be provided to perform the reentry. Cold gas thrusters, mono- or bi-propellants, solid, electric or hybrid propulsion systems are common [14].

A comparison of these major deorbting strategies is also found in [15].
Performing a controlled reentry without the need to provide any power is the most desirable case of the three, since the decommissioning system would barely impact

the cost of the mission, hence encouraging more agencies and commercial operators to widely adopt the guidelines and reducing the debris release rate.

Passive deorbiting is therefore an active field of research, and different solutions are currently being investigated.

1.4 E.T.Pack

E.T.Pack, short for *Electrodynamic Tether Technology for Passive Consumable-less Deorbit Kit*, is a FET-Open project founded by the European Union's Horizon 2020 Research and Innovation Programme whose goal is the full development of a spacecraft-independent deorbiting kit (DK) by mid 2022 and a future demonstration flight. The project is carried on by a consortium of six european partners, amongst which is the University of Padova.

The project's final goal is the realization of a commercially available deorbiting module, which would ideally be acquirable and mountable on compatible spacecrafts without the need of integration to the system, apart from the mechanical interface. Wide availability, low costs and no integration or design requirements could lead to broader adoption of deorbiting measures, lowering the on-orbit permanence time of spent or unused artificial bodies and thus mitigating orbital debris pollution and the possibilities of a collisional cascade.

The design of the DK consists of a scalable and independent module, with limited mass and volume impacts (total mass less than 5% of the host spacecraft, nominally less than 25 kg and 20 L), conceived to

> *autonomously deorbit a spacecraft of 500 kg from a Sun-synchronous orbit of 850 km altitude in less than 24 months*

with an allowable spacecraft mass ranging from 200 kg to 1000 kg [16]. As an independent and fully self-contained unit the module provides its own power storage as well as the cold gas propulsion subsystem used during initial separation from the spacecraft.

During operations, the DK propels itself away from the host vehicle, to which is connected by an inhomogeneous, multi-material tape; the detachment rate is dictated by a previously computed operation profiles aiming at obtaining the desired stable configuration. Once full deployment is achieved, the tether interacts with the plasma in the ionosphere, generating a resistive thrust without the need of consumables - i.e. propellant. A brief introduction to electro-dynamic tethers is given in Appendix A.

Deployment of the tether from the DK is mission critical, as the tape exit rate heavily impacts the final orbital configuration and its stability, and a partial or missed deployment would affect the success of the mission. Moreover, adoption of a flat tether (tape) instead of a round wire - choice due to its higher ability at collecting electrons and lower chances of failure due to orbital debris impacts [17] - poses strict constraints on the deployer mechanisms as well as to the coil storage and positioning. Two distinct tape deployment strategies are currently under evaluation by E.T.Pack teams:

- **Fixed spool**:
  a flat tape spool is stored in the DK, with the tape wrapped around; during deployment, the tape is pulled perpendicularly to the spool plane and extracted by a rotating guide (left in Figure 1.3). Within this configuration, the spool is stationary and the only moving part is the extractor; tape rewinding is not feasible, and the tape is twisted upon exit from the DK.
- **Rotating reel**:
  the tape is stored on a rotating wheel, and deployed by unwinding it on the spool plane with a pulleys assembly (right in Figure 1.3). Tape rewinding is feasible. With respect to the previous configuration, more moving parts are required (pulleys, rotating reel, reel brake) but more operational options are also available; moreover, the tape is not twisted with this latter approach.

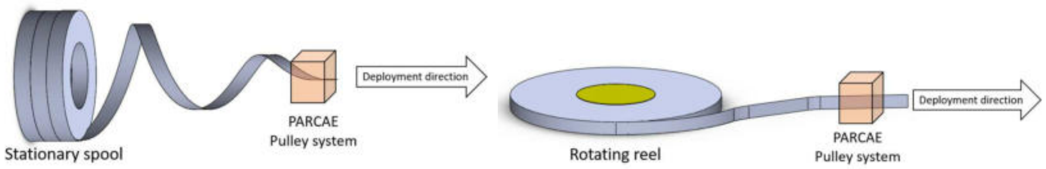

Figure 1.3: Graphical representation of the two tape deployment approaches.
Left: Fixed Spool. Right: Rotating Wheel.

Validation of the latter, the rotating wheel design, and experimental testing of its dynamical behavior in support of E.T.Pack team are the purpose of this thesis work. A down scaled mockup will be conceived and realized, and later tested in a dedicated low-friction testing facility.

1.5 Document structure

This document's organization and development flow is here briefly described; see Figure 1.4 for a high-level graphical representation.
Following this Introduction, some details about the current E.T.Pack design and the available testbed and testing facility will be given in Chapter 2, helping shaping requirements and constraints for the subsequent phases. Selection and sizing of Hardware and Software will be then tackled: the mechanical components of the system are treated in Chapter 3, while Chapter 4 focuses on the communication layer, the electronics and telemetry subsystem. Components and subassemblies have then be tested as described in Chapter 5 prior final assembly of the completed mockup.

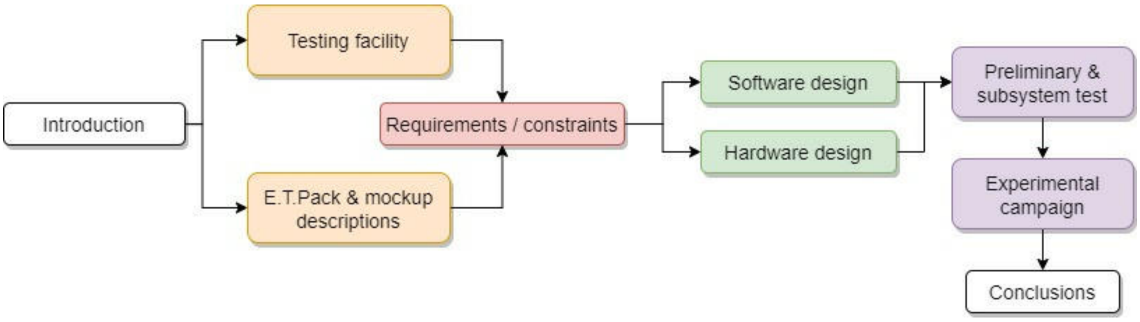

Figure 1.4: Logic flow diagram of the document.

Chapter 6 addresses the first experimental campaign: three preliminary characterization, deployment and reel-in tests have been performed and are here described. Chapter 7 finally concludes this document with some final observations and a global overview of the carried out work.

Chapter 2

Mockup and testing facility

The aim of the work is to validate the design developed by E.T.Pack team and to compare the observed behavior with the theoretical predicted one, thus providing useful information for the final flight configuration. For this reason, the mockup presented here must replicate E.T.Pack main features.
The initial testing campaign forecasted for E.T.Pack mockup includes thrust-vs-pressure characteristic curve determination, tape viscoelastic properties investigation, demonstrative deployment and reel-in procedures. Further tests will be evaluated and planned as the development proceeds.
An overview about the testing facility and the testbed is here presented.

2.1 Rotating Reel Prototype layout

As anticipated in Chapter 1, this work aims at building a mockup able to accurately replicate the real system behavior of the selected Rotating Reel configuration. The design and the system's layout are inherited by the E.T.Pack working group and are here described.
E.T.Pack general layout consists of a 40 cm diameter reel centered inside the deployer body, whose tape is feeded directly into the Pulleys, Actuator, and Roll Compression Assembly for E.T.Pack (PARCAE), the four-pulleys subsystem highlighted in Figure 2.1; PARCAE task is to impose the tape exit speed during the deployment phase, exert an holding torque to maintain a constant tape length or to guide the tape during reel-in operations. The whole pulleys assembly is critical to decouple the internal tether conditions from the external dynamics, subject to the interaction with the space environment and to the orbital dynamics in general.
Tape exit is at the middle of the body, to provide symmetry: asymmetrical tape positioning would exert torque on the deorbiting kit, affecting its attitude control

and the deployment angle.
The necessary deployment force is provided by aluminum-on-aluminum friction at the interface between the pulleys and the tape: it has been estimated that a preloading of around 15 N normal to the pulleys axis is enough to overcome the tape tension and the reel rotational inertia while still preventing the tape from slipping [1]. Preloading is achieved by two screws coupled with springs pushing on one of the pulleys bearings (see Section 3.2).

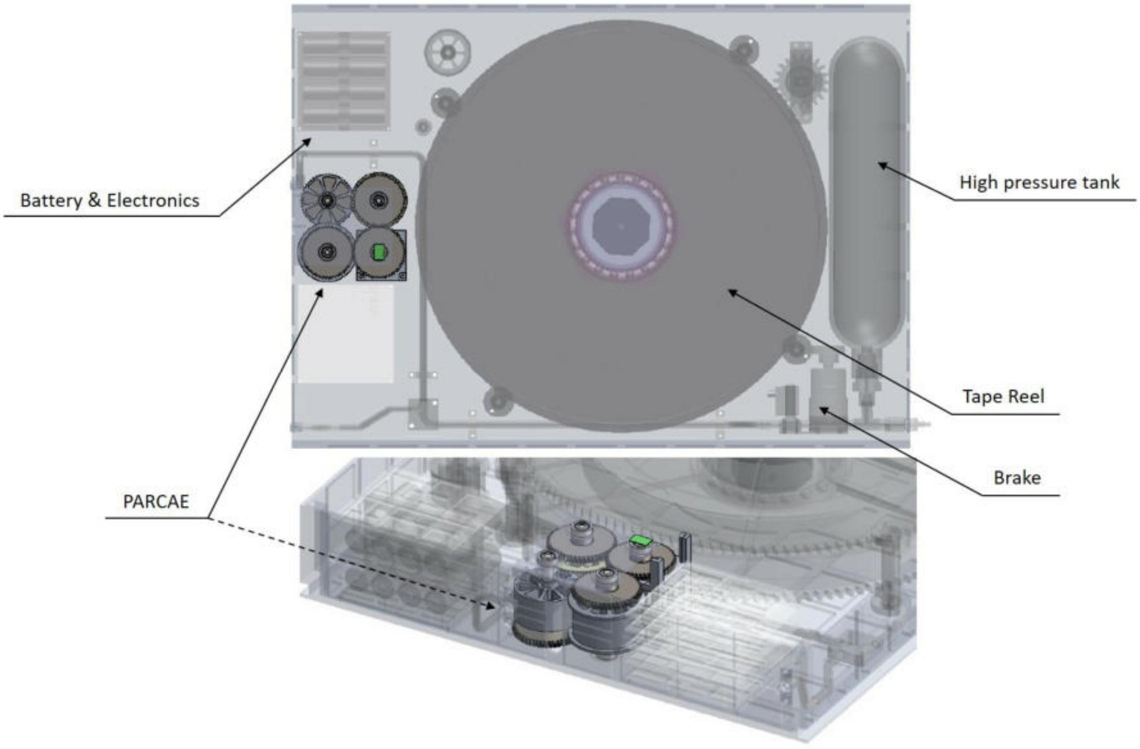

Figure 2.1: E.T.Pack global layout; Pulleys, Actuator, and Roll Compression Assembly for E.T.Pack (PARCAE) subsystem is visible and highlighted.

Coupled to the reel is the reel brake, needed to ensure a proper tape tension for the whole duration of the deployment: the tape exit velocity is a key parameter for the whole mission since it determines the orbital final configuration and is subject to changes as the development progresses; acceleration as well as deceleration phases must therefore be taken into consideration. Deceleration of the deployment could lead to the tape being unrolled at a rate greater than the desired one due to the reel high angular momentum, causing the tape to accumulate inside the deployer body; since this might lead to deployment failure - the tape could tangle on other

---

[1] Lorenzo Olivieri, personal communication, March 18, 2020

components, twist on itself, knot, etc. - proper braking moment must be provided to prevent the reel from freely rotating, while still allowing the rotation needed for the deployment. For the flight model a tension $F_T \in [0.1; 1.0]$N has been shown to be the right compromise between uncontrolled and free rotation [2].
Momentum during the first phases of the detachment from the host spacecraft is provided by two cold gas actuators, set on the deployment face. Thrust is needed to ensure a safe departure until the gravity gradient becomes not negligible.
PARCAE, the tape reel and the thrusters are the main features that are desired to be replicated in the experimental mockup.

2.2 Testing facility

Tests on the mockup will be performed on a low friction table at CISAS-UniPd facilities to simulate 3-DoF free motion (two translational axis on the table plane and the rotational one about the table normal) via an air cushion system, part of the SPARTANS test setup [18]. The original SPARTANS attitude module is replaced with E.T.Pack testbed, which will provide independent communication and power capabilities.

Information about the mockup position are gathered by SPARTANS external optical motion capture system (MC) based on IR cameras and reflective markers [19, 20], while telemetry data and testbed status (such as motors status, thrusters pressure and elapsed time) will be transmitted to the base station by the mockup on-board data handling and telemetry subsystem (see Section 4.2).
To simulate the presence of a massive host spacecraft, which shall be assumed fixed with respect to the deployment module and insensitive to the small tension exerted by the tether, the outer tip of the tape is fixed to a vertical post at one corner of the glass bed. An external load cell will be used to quantify the tension exerted by the tape on the post (i.e. to the host spacecraft).
Referring to Figure 2.2, the testing facility consists therefore of four main elements: a) the testbed itself, which will be later discussed; b) the glass-covered table to provide a low friction interface with the module, measuring 3m × 2m; c) an infrared MC system able of measuring and reconstructing the position of the testbed by means of reflective markers, and capable of measurements with σ values of less than 1 mm; d) one or more ground control stations.

---

[2] Lorenzo Olivieri, personal communication, March 18, 2020

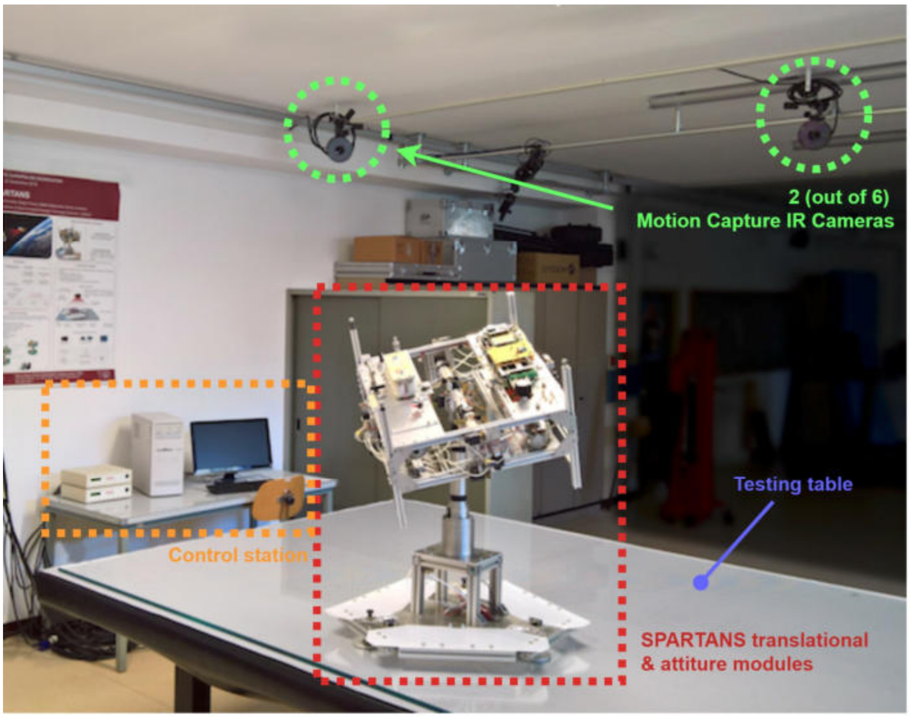

Figure 2.2: CISAS/UniPd SPARTANS testing facility.

2.3 Mockup

The mockup unit is in turn made up by two distinct components (see Figure 2.3): a) SPARTANS low friction module; b) E.T.Pack mockup, consisting of a cold gas propulsion subsystem and a tape deployment and control subsystem.

The E.T.Pack testbed consists of different subsystems, partially addressed by this document. Referring to Figure 2.4, the following main components can be identified:

A) High and low pressure pneumatic distribution subsystem.
B) High pressure cold gas tank.
C) Low pressure cold gas thrusters.
D) Tape reel and reel-brake interface gear (cfr. Section 3.6).
E) Reel brake (cfr. Section 3.5).
F) Control electronics, data handling and telemetry, bus voltage regulation (cfr. Chapter 4).
G) PARCAE assembly (cfr. Section 3.2 and 3.4).

Additionally, a load cell is planned to be used to measure internal tape tension between PARCAE assembly (G) and the rotating reel (D); its adoption is currently under investigation and mechanical as well as software interfaces have been arranged

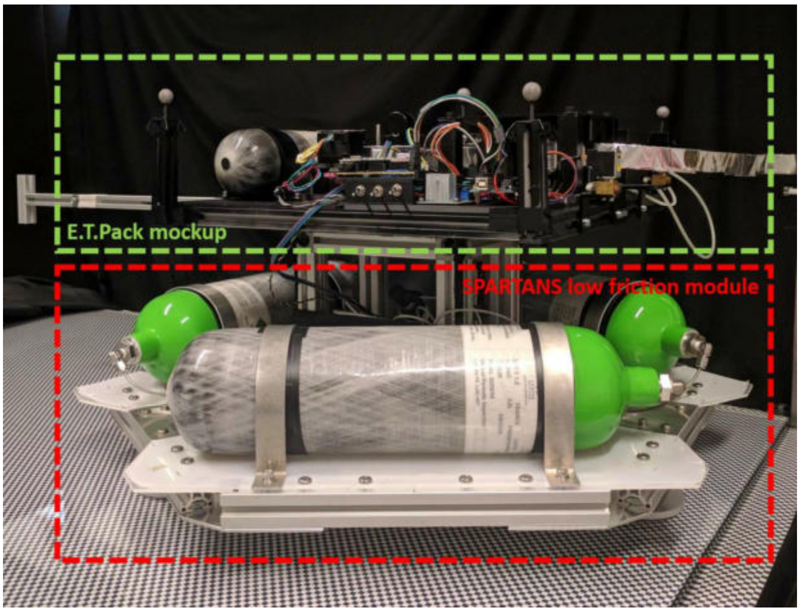

Figure 2.3: E.T.Pack testbed side view; SPARTANS low friction translation module (bottom) and E.T.Pack mockup (top).

in sight of its future addition.
The thrusters are designed to be symmetrically located with regards to the plane passing through the center of gravity of the mockup, and their position adjustable: since they can only fire simultaneously, no attitude control is as of now achievable, and symmetry is needed to achieve a null rotating torque on the mockup.

While SPARTANS translation module has already been developed [18–20], the remaining part is left to be designed, assembled and tested. The propulsion system has been realized by Lungavia, E. [21], and the deployment and control section is matter of this paperwork.
A control station is also needed to manage the testbed and the tests phases (deployment, rewinding, propulsion) and to gather and dispatch telemetry data and commands; data exchanges occur via a wireless network and all data is gathered during tests by a machine running MATLAB, to be easily later exported and processed. The control station and data relay system realization will be later discussed in sections 4.2 and 4.3.

2.4 Testing campaign

After preliminary subsystem tests to ensure a proper operation of both the mockup and the data acquisition infrastructure, an initial testing campaign is foreseen, aiming to prove critical capabilities and to validate the physical dynamic behavior ex-

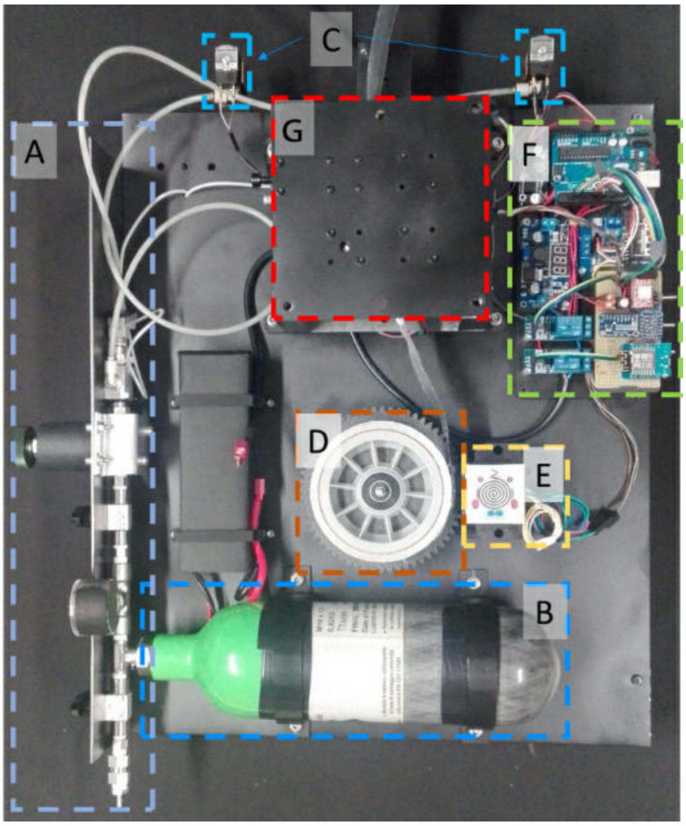

Figure 2.4: E.T.Pack testbed top view; the main components are highlighted and labeled.

pected for the testbed, and in turn for the real E.T.Pack deployer.
The following tests are planned to be run:

- **Thrust-vs-pressure characteristic curve determination**: characterization of the thrust produced as a function of the static feed pressure, which is expected to present a linear trend.
- **Tape viscoelastic properties investigation**: determination of stiffness k and dampening c values of the tape. Dynamic deployment simulations are heavily influenced by stiffness and dampening values, and is therefore highly desirable to possess accurate measurements of such quantities to obtain reliable results. While the stiffness can be estimated via analytical models of the system, the dampening presents high variability and unpredictability, and as such it must be empirically measured.
- **Deployment manoeuver**: main goal of the mockup is to replicate the deployment manoeuver following a planned acceleration and speed profile; the test aims at validating the work done by University of Padova's E.T.Pack team in terms of testbed dynamical behavior simulation, thrusters-tape interaction

evaluation and trajectory prediction.

- **Reel-in manoeuver**: a secondary test aiming at showcasing and evaluating the testbed capabilities of tape recovery and rewind; although not fundamental regarding E.T.Pack validation, such ability could open the way to further tests about tug operations [22], in orbit debris retrieval [23], rendez-vous [24] and more [25,26].

The initial testing campaign was carried out in August - September 2020. Further tests are being planned and evaluated and will be considered as the development proceeds.

Chapter 3

Hardware design

The first step to be taken in realizing the mockup is the hardware selection and sizing; mission objectives are qualitatively defined and translated in tangible and quantifiable requirements, being they functional, performance, or operational. Multiple possible configurations are then identified; investigating and comparing all possible solutions eventually leads to one being chosen as the optimal one, in terms of feasibility, cost, adherence to the requirements and overall ease of implementation. This Chapter focuses therefore on retracing all said design steps, aiming at obtaining a final feasible configuration.

3.1 Constraints and requirements

Developing a simple test-bed still representative enough of the real physical behavior of the system, able to produce valuable empirical results, casts different constraints and requirements: adherence to the real world assembly is required, while simplifications are needed for a mockup of reasonable complexity. Trade-offs will therefore likely be made in order to ensure the adherence to these two main constraints.

Mission driven requirements

E.T.Pack is being designed and developed by a consortium of international players; mission objectives and goals have been thoroughly discussed by team members, and it is not the purpose of this paperwork to exhaustively illustrate or motivate them. Mission related requirements will be therefore listed and partially discussed, and shall be accepted as they are.

- *The testbed shall deploy a* 25 mm *wide,* 30 µm *thick aluminum tape*
  E.T.Pack is planned to deploy a tape composed by two materials, a first plastic

section followed by a longer aluminum one; lengths will not be disclosed. To emulate the space segment, the testbed will have to deploy the same tape in terms of material and sizes.

- *The deployment speed of the tape shall be precisely controlled*
  Due to the orbital mechanics of tethered systems, the deployment speed is a primary factor coming into play into the angular stability and into the final state condition of the deployed tape. A specific final configuration is needed, therefore an accurate unwinding rate must be accomplished.
- *The tape shall be maintained tense*
  To prevent uncontrolled tape release, the tape must be tensioned, with a force estimated at about $F_T \in [0.1; 1.0]$N for the flight model [1]. Since the angular velocities and the reel angular inertia will be reduced in the test device, a new suitable tension range is to be imposed.

Testbed driven requirements

Limitations are posed by the experimental nature of the system, due to be tested in confined spaces and with limited resources; the following main constraints have been identified.

- *The testbed shall be able to represent the dynamics of the real system*
  Main goal of the whole mockup is to simulate the behavior that the actual deployer will exhibit once operational. Adopting different deployment strategies for sake of simplifying the design is not a viable solution, as this will lead to wrong or not representative behaviors and results.
- *The testbed shall respect the size constraints of the University testing facility*
  As already stated (see Section 2.2), tests will be performed on a low friction table which measures 3m × 2m; the model must therefore be able to fit and operate in the aforementioned dimensions. Moreover, since studying the behavior of the system during the deployment phase is of particular interest, longer-lasting deployments are desirable. The testing facility will be set up to observe the deployment along the table diagonal - giving a total length of ≈ 3.6m to work with - and the deployer itself should be as short as possible to leave out enough space to be able to move; a bulky deployer would take up space from the table and would leave out less room to move compared to a shorter one, restricting the testing abilities.
  A size constraint has therefore been set to be $l \leqslant 40$cm and $w \leqslant 30$cm.

---

[1] Lorenzo Olivieri, personal communication, March 18, 2020

- *The testbed shall be lightweight*

  Interface with the table will be provided via a compressed air layer cushion which ensures low friction and a 3-DoF free movement; to avoid overloading the pneumatic system, leading to higher pressures, bulkier and heavier tanks, shorter test times and an overall oversized model, the testbed must be weight efficient. This is not a strict requirement and no explicit values will be provided, anyhow useless weight and masses shall be avoided.

  Manufacturing of numerous components via 3D printing in PLA (standard FDM technology or SLS if higher accuracy is needed) will help in maintaining the total mass in the acceptable operational envelope.
- *The testbed shall be modular*

  One goal of the simulation is to be able to test different solutions to determine which one represents the best approach to the problem. Being able to swap out components without the need to radical changes to the system is key for a fast iterative design process; designing subsystems to be independent of each other allows for numerous modules to be planned and manufactured with the only constraints being posed on the interface, which must clearly be consistent. The same applies to software: writing modular functions is usually best practice and allows for easy and fast testing, debugging and maintainability of the source code, opposed to monolithic and cross-referenced code bases.

  The system must therefore be modular, hardware and software wise.
- *The testbed shall be easy to manufacture and assemble*

  Manufacturing and assembly will be performed in the University laboratory; avoiding complex parts, exotic materials and generally intricate design will allow faster and cheaper production with lower building time.

  As already reported, additive manufacturing should be used when possible to speed up the process.
- *The testbed shall be self-sufficient in terms of power*

  The module must be free from external power sources since its sliding action with absence of external interaction and forces does not allow for cables or connectors being run from and to the assembly; power must therefore be delivered via an on-board battery. Although power efficiency is not a concern - batteries can be changed on the go without issues - a good battery life is desireable to allow for multiple consequent test run being made.
- *The testbed shall permit for quickly repeatable runs*

  While testing the deployment procedures, numerous consequent runs will be performed to gather statistically meaningful data; the system must allow for an easy and fast restoration of the mockup to the initial state, either via the tape rewinding system or with a sort of fast reel detachment.

- *The testbed shall allow for the tape being rewound onto the reel*
  Aside tape deployment, which is the main objective of the testing campaign, reel-in capability is a secondary quest; demonstrating in-orbit tape retrieval - or simply building a system capable of such operation - could open up possibilities of tug and object retrieval operations testing. Moreover, the testing campaign will benefit of fast/automatic tape rewinding for consequent repeated tests.
- *The testbed shall provide the ability to adjust the preload force onto the pulleys*
  Pulleys preloading provides traction force transmission from the drive motor to the tape; lower contact forces would result in the tape slipping and not correctly deploying, while excessive ones could deform or damage the thin tape, or exert useless resistive torques to the aforementioned motor, resulting in higher power consumption or stall.
- *The testbed shall only use open loops*
  It has been shown that closing a feedback loop with on-board readings is complex and could lead to unwanted behaviors, mostly due to the sensors intrinsic inaccuracy. This applies above all to the internal tape tension planned to control the braking torque. Feedback loops are under investigation as far as the flight model is concerned, for both the development driver motor speed and the braking system, but must be avoided during the testbed design.

The design phase hereafter reported will therefore have to cope with the cited constraints.

3.2 PARCAE assembly

Pulleys, Actuator, and Roll Compression Assembly for E.T.Pack (PARCAE) is at the core of the mockup, as it allows the tape deployment at the desired speed, decoupling the inner dynamic from the outside disturbance environment; the assembly must be stiff enough to prevent deformations or relative motion, allowing at the same time for a preloading to be exerted on the pulleys to increase contact pressure, thus preventing tape slippage. As visible in Figure 3.1, PARCAE is composed of three pulleys: the two gray ones are driven by the drive motor, and draw the tape by means of friction, while the yellow one is freely rotating and is used to guide the tape from the reel.

Since fidelity to the original PARCAE concept is needed to provide meaningful experimental data regarding its behavior, the subassembly has been faithfully repli-

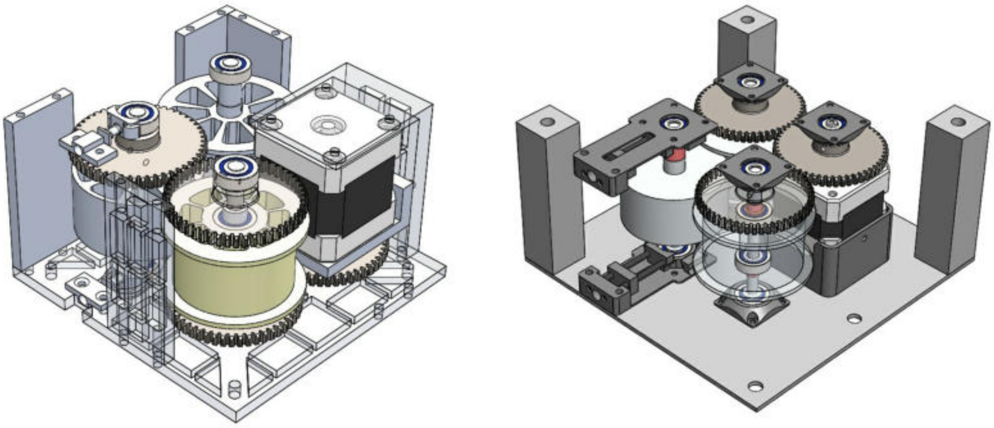

Figure 3.1: PARCAE flight model (left) versus the test assembly (right).

cated: pulleys radius and size match with the planned ones, as well as relative positioning of all components. Off the shelf products are preferred above custom made ones to spare time and financial resources during development. Bearing fixtures and the preloading mechanism are obtained via 3D printing technologies instead of being carved off the bottom aluminum plate.

Pulleys preloading

To achieve variable contact force between the traction pulleys and the tape a preloading system is built into PARCAE: two sideways screws push onto four springs, compressing them, which in turn exert a force onto the pulley bearings proportional to the total springs displacement. The system allows to control the contact force between pulleys and tape, therefore the friction, and finally the maximum tape tension the system can stand without slippage; clearly, higher friction between pulleys results in more power being requested to the motor to drive the whole assembly, and therefore a tradeoff is required.

3.3 Dynamic simulation

In order to properly size the needed components, the dynamic of the testbed during a braked deployment or during reel-in must be simulated. MATLAB scripts have been written implementing a dynamic model of the deployer. For such simulations, the pneumatic thrust subsystem or SPARTANS floating module have been neglected, taking only PARCAE deployer and the reel assembly into consideration. The main torques acting on the system formed by the reel, the tape and the pulleys are due to the reel rotational momentum, the driver motor torque (acting on the reel via the tape tension), the brake torque, and resistive torques acting on the bearings, and are schematized in Figure 3.2.

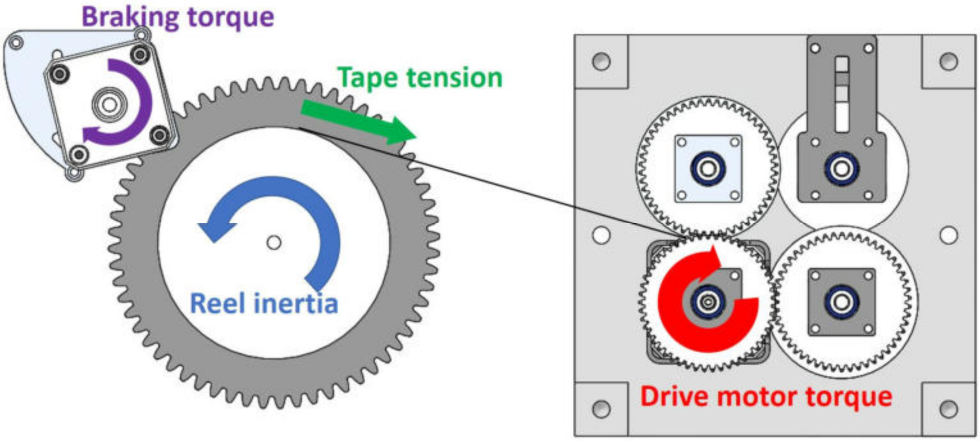

Figure 3.2: Representation of the main torques acting on the tape subsystem.

During simulations, the unwinding profile has been imposed as a sequence of the mockup linear acceleration, coasting and deceleration and fed into an ODE45 integrator to obtain position and speed vectors as a function of the elapsed time, as shown in Figure 3.3. These profiles replicate the ones planned for the space mission [27], consisting in roughly an initial speed up, a constant speed deployment and a final deceleration, and are scaled down at about one third to meet the testing facility constraints, hence providing longer test runs on the limited table space. For the particular case shown, the imposed profile consists of:

a) constant acceleration $a_1 = 0.007\,\mathrm{m\,s^{-2}}$ for $0.7\,\mathrm{m}$
b) coasting ($a_2 = 0\,\mathrm{m\,s^{-2}}$) for $0.8\,\mathrm{m}$
c) constant deceleration $a_3 = -0.01\,\mathrm{m\,s^{-2}}$ for $0.5\,\mathrm{m}$

resulting in a total travel - i.e. total deployed tape length - of $2.0\,\mathrm{m}$.
The deployment speed is computed from the mockup translational speed: considering the tip of the tape to be fixed with respect to the table (i.e. the external reference system), the exit speed of the tape is equal and opposite to the mockup speed. Knowing the deployment pulley radius, the rotational speed required to the drive motor is simply:

$$\omega_{stepper} = \frac{v_{tape}}{R_{pulley}}$$

and similarly for the stepper position and acceleration.

To estimate the torque exerted by the reel due to its angular momentum, the

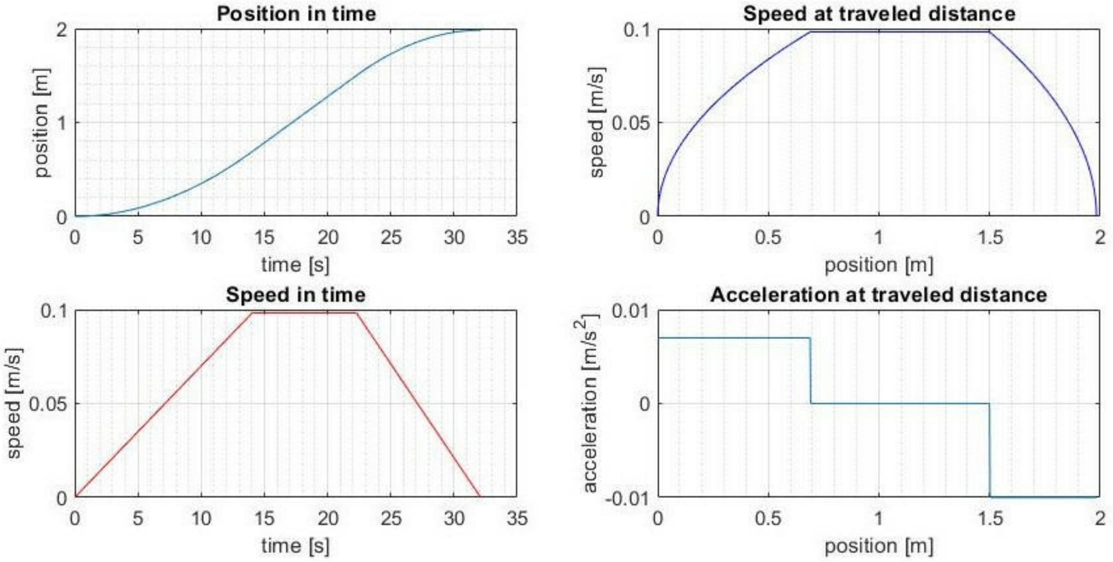

Figure 3.3: Mockup translational speed and acceleration derived from the imposed acceleration profile.

reel inertia must be known; it has been estimated using a 3D modelling CAD software (SOLIDWORKS) as a composite body of PLA (the large geared profile) and aluminum (the rolled up tape), resulting in an inertia of

$$I_{reel} = 3.697 \cdot 10^{-4}\mathrm{kg} \cdot \mathrm{m}^2$$

The reel rotational acceleration has been computed from the knowledge of the tape speed profile: given the radius $R_{reel} = 0.08\mathrm{m}$ as the distance of the tape from the reel center, the reel acceleration is, as shown before,

$$\dot{\omega}_{reel} = \frac{a_{tape}}{R_{reel}}$$

The torque due to the reel rotational momentum is now computed from Euler's rotation equation:

$$\vec{T}_{ext} = \frac{d\vec{H}}{dt} = \dot{\vec{H}} + \vec{\omega} \times \vec{H} \tag{3.1}$$

which substituting $\vec{H} = [I_o]\,\vec{\omega}$, and considering the inertia matrix I_o to be constant in the reference frame, becomes

$$\vec{T}_{ext} = [I_o]\,\dot{\vec{\omega}} + \vec{\omega} \times [I_o]\,\vec{\omega} \tag{3.2}$$

When $\vec{\omega} \parallel \vec{H}$, and if taking into account only the Z component, it yields to

$$T_{reel} = \dot{\omega}_{reel} \cdot I_{reel} \tag{3.3}$$

This equation gives the torque seen at the reel due to accelerations or decelerations, which then equates to the minimum amount of resistive torque the brake motor must provide in order to avoid uncontrolled reel rotation with a null tension. This value is particularly low, therefore braking can be achieved with any of the later on mentioned strategies (see Section 3.5).
Subsequently the torque due to the tape tension can be computed as

$$T_{tape} = F_{tension} \cdot R_{tape}$$

where the tape tension is currently unknown. Writing the torque balance equation and solving for the tension yields to the desired result:

$$\begin{aligned} T_{reel} = \dot{\omega}_{reel} \cdot I_{reel} &= T_{tape} - T_{brake} - T_{bearings} \\ \dot{\omega}_{reel} \cdot I_{reel} &= F_{tape} \cdot R_{tape} - T_{brake} - T_{bearings} \\ F_{tape} &= \frac{\dot{\omega}_{reel} \cdot I_{reel} + T_{brake} + T_{bearings}}{R_{tape}} \end{aligned}$$

where $T_{bearings}$ is the assumed friction torque on the reel axis, imposed as

$$T_{bearings} = 1 \cdot 10^{-4} \mathrm{N\,m}$$

Rigorously speaking, the braking torque is still an unknown. For a preliminary design it has been arbitrarily imposed equal to a value deemed possible, obtained from an inquiry conducted among different brake candidates, and adjusted for the gear ratio between the motor shaft and the reel. The used value is therefore

$$T_{brake,reel} = \frac{T_{brake,shaft}}{k_{GB}}$$

being $k_{GB} = 1 : 3$ the gear reduction ratio between the brake shaft and the reel and $T_{brake,shaft} \approx 1 \mathrm{mN\,m}$.
The tape tension acceptable range has been reduced to $F_T \in [0.05; 0.5]\mathrm{N}$ from the flight model $F_T \in [0.1; 1.0]\mathrm{N}$ range; this will allow the adoption of smaller motors to cope with lower tensions, while still ensuring the absence of uncontrolled unwinding. While lower tensions only result in smaller braking torques and are therefore accepted, higher tensions could lead to tape damages; only downscaling the constraints reported in Section 3.1 is hence permitted.
The main assumption performed during the dynamic simulation is that the reel always follows the imposed acceleration and speed profile, namely the drive motor inside PARCAE assembly has enough torque to assure the deployment. Said assumption allows to consider the reel and brake subassembly as independent from PARCAE, thus leading to lighter equation systems. This follows from what cited in

Section 2.1: PARCAE pulleys assembly is designed to decouple the internal dynamics from the outside environment and the deployed tape behavior, thus obtaining a more stable system.
The design is then iterated until a good configuration is achieved: once the brake has been sized, its true torque output can be fed into the relation, computing the tape tension; if this were to be lower or higher than acceptable, the brake choice must be repeated. Since the tape tension is a function of the braking torque, and the driver motor must account for it, the driver motor sizing (see Section 3.4) must be repeated - or checked - every time a new brake configuration is evaluated. This is not true the other way around: as long as the driver motor provides a sufficient torque to assure the deployment and to overcome the braking torque, no design iteration is needed.

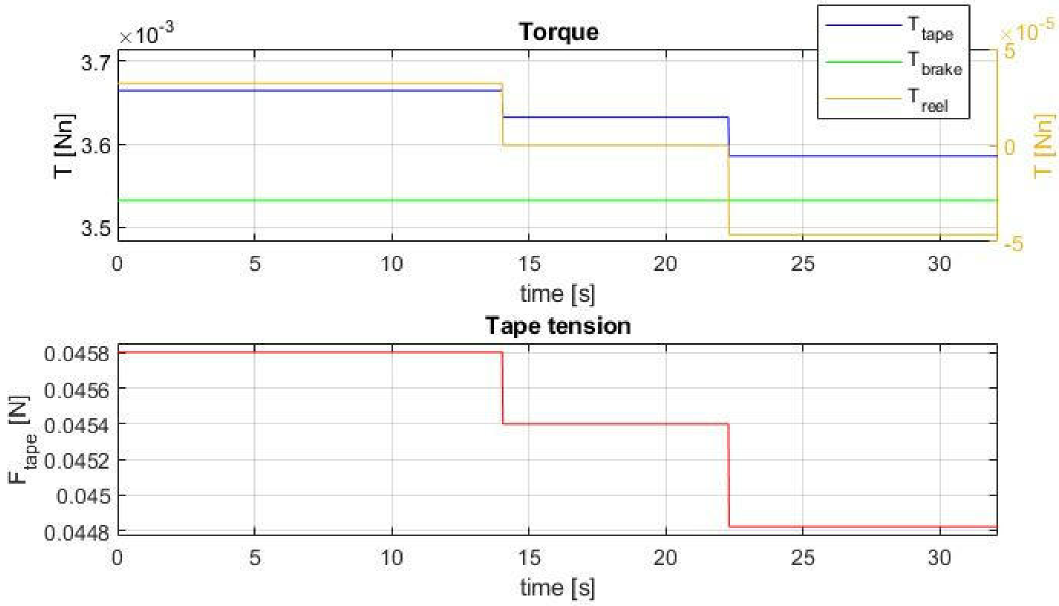

Figure 3.4: Torques acting on the reel (top): note how the inertia-induced torque is significantly lower than the others by two orders of magnitude; tension of the tape (bottom) mainly due to the braking torque.

As previously noted, the value of the momentum-induced torque is small compared to the other players: although the angular acceleration $\dot{\omega}_{reel}$ of the reel can vary with different deployment profiles, its impact is negligible, therefore the simulation is not to be remade for every profile change.
It is worth noting that the tape radius has been considered constant during the deployment phase: this is an assumption based on the fact that the amount of deployed tape ($\approx$ 2m) is small compared with the total rolled up length, implying

that both the reel inertia and the reel radius will not vary significantly over time. This assumption cannot be made for the real flight model, for which the variation of inertia and radius must be taken into consideration.

The simulated behavior of the system for the speed profile shown in Figure 3.3 is reported in Figure 3.4. Note how the inertia-induced torque (yellow) is small compared to the total torque (i.e. sum of acting torques) and varies sign according to the acceleration/deceleration phase.

The speed profile here considered is one of the many tested on the mockup, but represents the worst-case scenario, i.e. contains the maximum acceleration and speed that the mockup will be likely required to face, and is used to size the components for the maximum allowed load. Actual testing conditions will therefore vary from the one here shown.

Following the here predicted behavior hardware components - drive motor and brake - are later discussed and sized.

3.4 Driver motor selection

The selection of the driver motor is straight forward, as the requirements on deployment rate precision coupled with the absence of a feedback loop cast strong constraints on the choice. Below a brief explanation of the rationale behind the final choice is reported, together with the motor sizing and some notions about the control logic.

For the task, DC, BrushLess DC (BLDC), servos and stepper motors have been taken into consideration during the preliminary selection. BLDC and DC motors, and therefore servo motors as well, have been found to offer higher yields, i.e. higher torque per ampere at a given speed, or higher speeds at fixed loads, therefore their adoption is worth considering.

A comparison between two of the motors later used on the prototype is performed: DC motor `RS 413-0622`, coupled with a 1:100 planetary gear reduction, and stepper motor `RS 42SH47-4A` nominal values are reported and confronted in Table 3.1.

A first comparison can be executed on the motors efficiency: at maximum efficiency point, the DC motor provides an output power of

$$P_{out,DC} = \omega \cdot T = 6.953[\mathrm{rad\,s^{-1}}] \cdot 0.1864[\mathrm{N\,m}] = 1.31\mathrm{W}$$

with an input power of

$$P_{in,DC} = V_{in} \cdot I_{in} = 12[\mathrm{V}] \cdot 0.194[\mathrm{A}] = 2.328\mathrm{W}$$

	Torque	Speed	V_{in}	A_{in}
`RS 413-0622` DC motor	$19.2\,\mathrm{g\,cm^{-1}}$	$6636\,\mathrm{rpm}$	$12\,\mathrm{V}$	$0.196\,\mathrm{A}$
with 1:100 gear reduction	$0.186\,\mathrm{N\,m}$	$66.4\,\mathrm{rpm}$		
`RS 42SH47-4A` stepper	$\approx 0.42\,\mathrm{N\,m}$	$66.4\,\mathrm{rpm}$	$2.8\,\mathrm{V}$	$1.68\,\mathrm{A/phase}$

Table 3.1: DC vs. stepper motor comparison. DC motor values are taken at the point of maximum efficiency as reported by the datasheet.

The efficiency can then be derived, and is found to be equal to

$$\eta_{DC} = \frac{P_{in,DC}}{P_{out,DC}} = 0.56$$

Note that the assumption of an ideal gear box with unitary yield has been made, therefore transmission losses are neglected. The same applies for the stepper motor, the only difference being that the given amperage is *per phase*; when driving the motor in *full steps mode* both phases are turned on simultaneously, effectively doubling the drawn current. More insight about stepper driving techniques is given in Section 3.4.1.

The efficiency of the motor can be assessed as for the DC case:

$$P_{out,step} = 6.953[\mathrm{rad\,s^{-1}}] \cdot 0.42[\mathrm{N\,m}] = 3.41\mathrm{W}$$

$$P_{in,step} = V_{in} \cdot I_{in} = 2.8[\mathrm{V}] \cdot 2 \cdot 1.68[\mathrm{A}] = 9.41\mathrm{W}$$

yielding to a theoretical efficiency of

$$\eta_{step} = \frac{P_{in,step}}{P_{out,step}} = 0.36$$

It is noticeable how DC motors delivers higher efficiency with respect to steppers, and should therefore be considered the prime candidate for the task; moreover, DC motors offer other advantages, such as requiring an input power proportional to the attached load and providing a non-incremental, smooth motion. Stepper motors on the other hand require a fixed input current proportional to the nominal tension and the coil resistance (from Ohm's law $V = RI$) and move in an incremental fashion, with a step size dictated by the core physical construction [2].

Nonetheless, DC motors can not be picked due to mission constraints: speed control on DC/BLDC motors must be obtained through the use of a closed loop feedback

---

[2] As reported in Section 3.4.1, stepper motors can move a fraction of their step size if controlled with specific techniques. In this case torque is lost in favor of angular accuracy.

system; multiple approaches are available, from simply gauging the rotation rate by means of mechanical or magnetic rotary encoders, to theoretical ones, based on measuring the input current and comparing it with a mathematical model [28]. Since feedback loops are not accepted as per requirements, stepper motors are picked as the only feasible alternative, thanks to their intrinsic property of being able to provide open loop positioning and speed control.
Continuous rotation servo motors could also fit the job, providing precise speed and positioning by means of an integrated closed control loop. They moreover bring the advantages of DC motors, as moving continuously without incremental steps and not requiring a constant current, being the input power load-dependent. However, it has been found that, for the required torque and speed combination, stepper motors are cheaper than continuous rotation servos; also, a stepper motor could be fit into PARCAE assembly without the need of an additional geared redaction, whilst a servo motor would need one - external or internal - making the drive subassembly bulkier and possibly preventing it from fitting in. Lastly, the original E.T.Pack configuration adopts a stepper motors as the driver motor of choice: considering all trade-offs so far cited, it is convenient to select a stepper motor as the drive unit, respecting all constraints and sticking with the original E.T.Pack concept.

Motor sizing

Sizing the drive stepper motor is not a trivial task, as many of the involved resistive torques should be experimentally evaluated or do not have an immediate definition. These are mainly the rolling friction between PARCAE pulleys and parasitic torques of the bearings and the gears. In addition, the known torques due to the tape tension and to single bodies angular accelerations (T_{eul}) must be accounted for.
The estimated total torque the drive stepper motor is due to overcome is therefore

$$T_{drive} = T_{tape} + T_{eul} + T_{fric}$$

where T_{tape}, the torque due to the tape tension acting onto the pulley, is trivially computed as

$$T_{tape} = F_{tape} \cdot R_{pulley}$$

with $R_{pulley} = 0.025\text{m}$ being the pulley radius. From the already cited dynamic simulation the maximum value is found to be

$$T_{tape,max} \approx 1.1 \cdot 10^{-3}\text{Nm}$$

Now T_{eul}, the Eulerian torque due to bodies angular acceleration, is estimated with the previously cited equation

$$T_{eul} = \sum_i I_i \cdot \dot{\omega}_i$$

as the sum of the contribution of all rotating bodies coupled to the motor. Since the reel rotational inertia is accounted for in the tape tension computation, and neglecting the gear ratios between the pulleys - PARCAE pulleys all have a gear ratio of $k_{GB} = 1 : 1$ - the sum is reduced to

$$T_{eul} = 3I_p\dot{\omega}_p + 4I_g\dot{\omega}_g$$

where ω_p and I_p are pulleys inertia and rotational speed, while ω_g and I_g refer to the gears. The equation takes into consideration all moving parts of PARCAE, namely three pulleys and four gears; pulleys angular acceleration is obtained from $\dot{\omega}_p = \dot{\omega}_g = \frac{a_{tape}}{R_{pulley}}$ and the moments of inertia are gathered from the CAD model, in which the relative geometry and material properties are imposed.
The resulting value is dependent from the speed profile, and is

$$|T_{eul,max}| \approx 1.03 \cdot 10^{-4}\mathrm{N\,m}$$

for the one reported in Figure 3.3.
Friction torque T_{fric} can be partially estimated as rolling friction between two aluminum surfaces as in the work by Offner et al. [29]:

$$T_{fric} = \mu R g F_N = 1.83 \cdot 10^{-3}\mathrm{N\,m}$$

where $F_N \approx 15\mathrm{N}$ is the preloading force perpendicular to the rotation axis, $\mu = 0.0005$ the coefficient for aluminum-on-aluminum interaction.
All together, the foregone required torque is about

$$T_{drive} \approx 3.1 \cdot 10^{-3}\mathrm{N\,m}$$

It is clear how the theoretical computed values produce an almost negligible contribution with respect to the output torques of the aforementioned motors.
Offner's relation predicts rolling friction for smooth surfaces and rigid bodies; however, deformable and partially corrugated aluminum tape has been applied on PARCAE pulleys to increase contact with the tape and prevent slippage. It has been found that its presence heavily impacts on the rolling friction torque (see Section 5.1.3), but could not be analytically estimated. Moreover, friction due to the pulleys axis rubbing onto PARCAE chassis and between the gears - due to imperfect pivot positioning - has been observed. Therefore, higher torques are to be requested to

the driver motor to ensure enough power is delivered to the pulleys assembly.
Two stepper motors with more than adequate torque have been selected for further testings: stepper motors `RS 42SH47-4A` and `RS 1805279`. Relevant nominal values are reported in Table 3.2.

	T_{hold}[N m]	V_n[V]	I_n[A] (per phase)
`RS 42SH47-4A`	0.44	2.8	1.68
`RS 1805279`	0.16	12	0.31

Table 3.2: Selected drive motors characteristics.

These two motors have been chosen for different reasons: in the first place, their output torques are higher than what has been predicted as necessary, with plenty head room for model `RS 42SH47-4A`; secondly, they present different nominal tension values, which allows for testing of various drive techniques (see Section 3.4.1) on the testbed 12 V regulated bus.
In Table 3.2, holding torques (i.e. torques exerted when the motor is stationary) have been reported; when in rotation, stepper motors output slightly decreases with speed increase, but can be considered constant in certain speed interval (see the plateau in Figure 3.5), therefore, if working with low enough speeds, the output torque can be taken as a constant slightly lower then the holding one.
In Section 5.1.3 both motors are tested and compared, and the definitive selection is proposed.

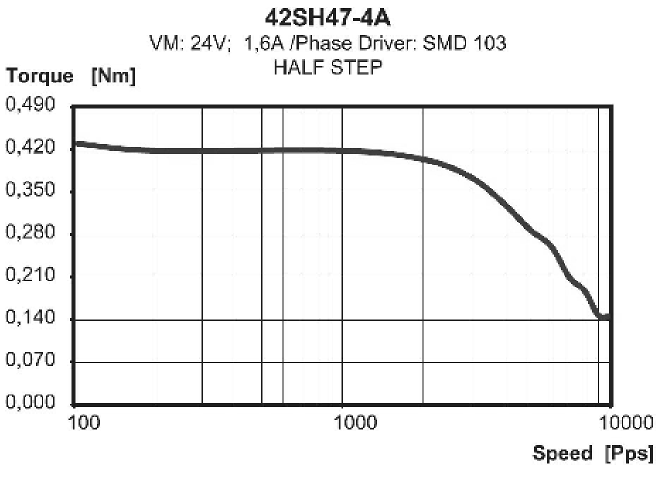

Figure 3.5: Stepper motor `RS 42SH47-4A` speed-torque characteristics provided by the datasheet.

3.4.1 Stepper motors driving techniques

A brief insight about stepper working principles and driving techniques is here proposed; since the in-depth discussion of these topics is not the focus of this paperwork, see [30] for a description of the principles of stepper motors operation or [31] for details about stepping and microstepping.
Stepper motors rotors are permanent magnets composed by two toothed rows of opposite polarity shifted one by another by the size of a teeth; the stator is made of two alternating phases (see Figure 3.6). By providing current to the phases following an alternating pattern, rotor movement is induced, one step each current polarity inversion. The step size so obtained is function of the teeth count: common stepper motors present 200 teeth, resulting in a step size of $\Delta\theta = \frac{360°}{200} = 1.8°$. Aligning the rotor teeth with the stator grooves by energizing both phase simultaneously with the same current modulus is defined *full stepping* and is the more easily achievable motion, but implies low angular resolution.

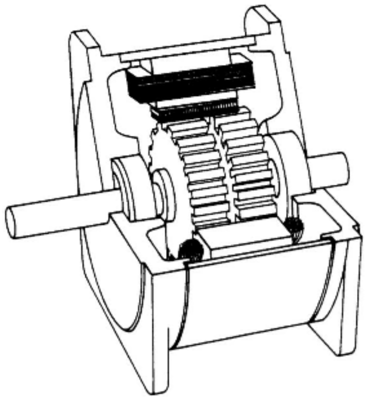

Figure 3.6: Sectional drawing of a stepper motor; at the center is visible the toothed rotor.
Source: Bodson et al. [32]

Shaft angular accuracy can be improved by controlling the current flowing to each phase, positioning the teeth mid-way between two adjacent stator grooves, rotating the rotor by a fraction of the default step size. This strategy is named *microstepping* and is usually offered by motor controllers in steps of a power of 2, and therefore the following microstepping resolutions are commonly found:

$$1 \qquad \frac{1}{2} \qquad \frac{1}{4} \qquad \frac{1}{8} \qquad \frac{1}{16}$$

where resolution 1 means full stepping, with both phases equally energized. As reported in [31], microstepping is achieved by replicating a sinusoidal wave with the two phases currents, and can not be replicated with basic controller such as an H-bridge.

Two driver boards have been chosen to drive the steppers: an `H-bridge L298` motor driver board and a `A4988` driver chip. While the first one is only capable of full step drive, the latter can be configured to reach $\frac{1}{16}$ microstepping; moreover, distinction must be made for the feed voltage: steppers nominal tension is computed to ensure that the maximum current flowing through each phase is the nominal one when fed with a constant voltage, from the well-known $V_{in} = R_{ph}I_{ph}$, where R_{ph} is the phase resistance. When using the `L298`, current intensity can not be controlled, therefore the maximum allowed tension is the nominal one; if using a dedicated chip instead - like the `A4988` - the current can be limited to its nominal value via *chopping* [3], allowing for higher input voltages. Benefits of chopping are faster motor reaction and a wider allowable input voltage range.

Regarding the motors reported in Table 3.2, considering that the mockup bus is at 12 V, motor `RS 1805279` can be operated directly with an `L298`, while stepper `RS 42SH47-4A` must be driven with a current chopper chip, or on a lower voltage regulated bus, to prevent coil damage.

3.5 Brake selection

In order to keep the tape tensioned whilst performing a deployment manoeuver, a brake must be adopted to provide a resistive torque to the reel shaft, as reported in Section 3.3. Three solutions capable of providing a predictable or adjustable torque have been evaluated for this application:

- Passive viscous dampers: compact - and cheap - devices that dissipate energy as heat via viscous interaction with a thick fluid, as silicone fluid. The provided torque is predictable but not adjustable (see rotational damper `ACE FDT-47` as an example [33]).
- Friction brakes: it has been shown that a predictable passive brake for tethers with circular sections can be obtained by wrapping the tether itself about a shaft a given number of turns; the turns number controls the braking force [34]. This approach, named *barberpole brake*, is elegant and less prone to errors and has already been used in space missions (see the YES2 demonstrative mission [1]).

---

[3] Choppers are DC to DC transformers converting a fixed DC voltage to a variable one by performing PWM on the output; the mean current can be controlled by varying the duty cycle, and can therefore be limited by the user.

- Braking motors: motors are, intrinsically, braking devices, as they generate an inverse potential difference across their leads proportional to the shaft speed, opening the possibility to modulate the resistive load. Moreover, current can be fed into the motor coils, actively braking the connected load and generating higher resistive torques. Multiple approaches to braking motors are therefore available, and will be later discussed.

Figure 3.7 showcases two of the cited braking strategies.

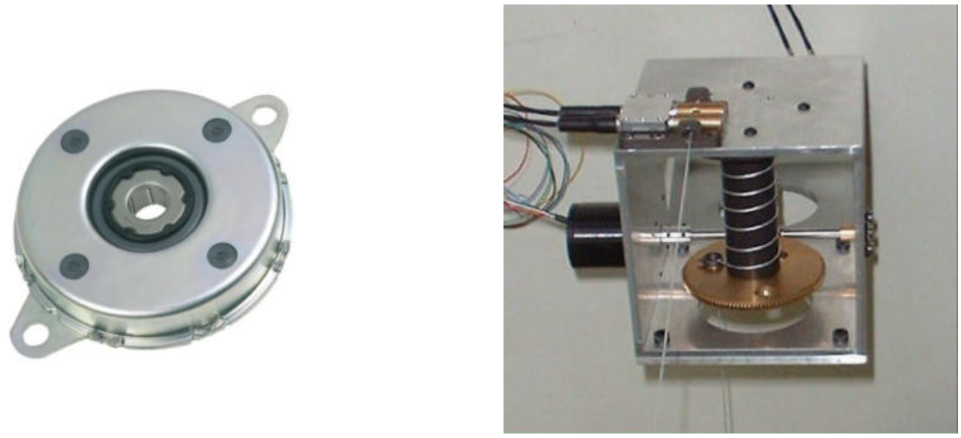

Figure 3.7: Passive viscous damper (left); a barberpole-style brake used by the YES2 mission [1] (right).

Of the three options here cited, braked motors have been preferred, as they can act as passive and adjustable brakes by exploiting the generated voltage across the leads [35, 36], and can be used as active brakes by energizing the coils, obtaining higher torques. In addition, a brake motor can be powered to drive the reel, hence rewinding the tape.
Motors can therefore satisfy to the tape tension and the tape rewinding requirements at the same time, whilst requiring only one component to accomplish both. Two different motor typologies have been considered and investigated and are here reported.

DC motors

Ranging from cars to attitude reaction wheels, DC motors have often been used to act as brakes, both passively and actively. During active braking, the coils are energized with an opposite polarity with respect to the one needed for motion, thus inducing a resistive magnetic field; passive braking is obtained instead by taking advantage of the induced voltage, employing the motor as a generator and forcing

the self-produced current to generate the needed resistive torque [37,38].
Regardless of the drive strategy, the main equations governing a DC motor are:

$$T = k\Phi \cdot I \qquad\qquad E = k\Phi \cdot \omega \tag{3.4}$$

that is, shaft torque is proportional to the fed current and armature voltage is proportional to the shaft speed. The term $k\Phi$ is composed by the *flux* of the motor ϕ and geometric factor k, which sums up internal electrical and geometrical properties; $k\Phi$ is constant for motors without field-weakening.
Considering a basic circuit, in which the motor is schematized as an ideal voltage generator E in series with coil resistance R_{mot} and coil inductance L_{mot}, and powered by a voltage generator V, (see Figure 3.9a) it can be stated

$$v(t) = e(t) + Ri(t) + L\frac{di(t)}{dt} \tag{3.5}$$

During steady operations it can be reduced to

$$V = E + RI \tag{3.6}$$

which yields, after some basic algebra by substituting equations 3.4 into 3.6, to

$$T = \frac{k\Phi}{R}V - \frac{(k\Phi)^2}{R}\omega \tag{3.7}$$

This relation represents the main equation describing DC motors working principle. Considering $k\Phi$ and R constant for a given motor and load, and a fixed input voltage V, the law represents a line with negative slope in the Cartesian plane: shaft torque decreases with increasing speed when used as a regular motor. Referring to equation 3.7, by reversing the polarity of either V or ω, different operational behavior can be achieved.

In Figure 3.8 the obtainable behavior are illustrated with reference to the $\omega_m - T_{em}$ Cartesian plane; common use case is *motoring in forward direction*, in which the motor drives a load thus providing mechanical and absorbing electrical power.

DC braking

When used as a brake instead, the behavior varies based on the braking strategy.
If fed with an input voltage lower than the one needed to sustain motion at the given speed ω_{mot}, the torque at the shaft will decrease, effectively generating a braking torque; this is achieved only when actively driving the motor, which is not the case to be considered here. This technique is known as *dynamic braking* or, with reference

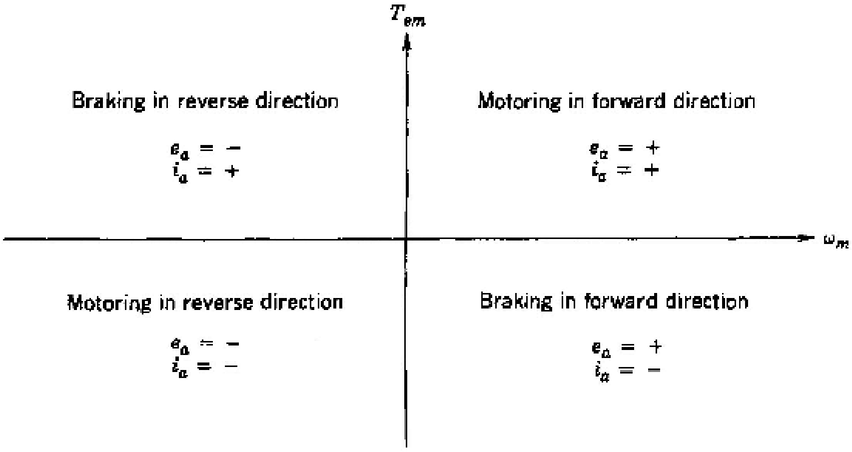

Figure 3.8: DC motor four-quadrant operation
Source: *Power Electronics: Converters, Applications,and Design* [39]

to Figure 3.8, *braking in forward direction.*
As already cited, a second option is to reverse the input voltage polarity, resulting in the so-called *plug breaking*: from the DC motor equation 3.7, considering V as the modulus of the the feed tension, the torque at the shaft will equate to

$$T = -\frac{k\Phi}{R}V - \frac{(k\Phi)^2}{R}\omega$$

effectively resulting in a negative torque. Input voltage could now be modulated to achieve the desired braking. This approach is certainly viable and allows for precise torque determination, but requires power to work; in power-restricted applications, such as spacecrafts, in which it is crucial to spare resources, dissipative or regenerative braking is to be preferred.

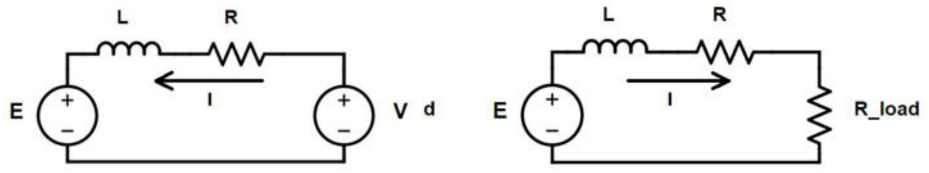

(a) DC motor during normal drive operations

(b) DC motor during dissipative braking

Figure 3.9: Schematics of the equivalent circuit for DC motors during drive or brake operations.

Regenerative or dissipative braking is obtained when the applied voltage is null, i.e.

$V = 0$V (Figure 3.9b). Power received through the shaft is used against the motor itself by shorting the leads or connecting them to an external passive load: the generated voltage induces a current inversely proportional to the total resistance R, thus generating torque. From the aforementioned equation the torque is

$$T|_{V=0} = -\frac{(k\Phi)^2}{R}\omega \tag{3.8}$$

which is directly proportional to the load speed ω. This makes the motor a viscous damper, and it follows that the generated torque is negligible when the speed is low, and clearly null when stationary.

Torque manipulation is feasible via the value of the resistance R: adding resistors in series with the motor raises R, thus lowering the torque; the maximum obtainable torque is given when R is at its minimum, i.e. when the only resistance in the circuit is the one of the motor coils, that is, when the motor leads are shorted.

If an external load is added, two different configurations can be generated:

- **Regenerative braking**, obtained when the external load is a battery; the current flowing from the motor recharges the battery, which represents a resistive load from the motor side. Benefits are the conservation of the energy inside the system (net of Joule losses) for later use, and reduced heat output; however, depending on the battery type, this configuration could need a battery charger circuit and/or a cell balancer. Moreover, braking is obtained only when the motor output voltage is higher than the battery voltage; if it were lower, the current flux direction would be inverted, resulting in power flowing from the battery to the motor, thus actively driving it. Being the output voltage proportional to the shaft speed this represents a problem in low speeds scenarios, if no boost converter is used.
- **Dissipative braking** follows the same approach, but uses a simpler power resistor to waste the power as heat. There is no lower limitation to the output voltage, since the passive resistor cannot feed the motor.

In both configurations, torque control is viable via PWM at the leads: varying the duty cycle of a short circuiting switch varies the mean tension, thus the current effectively passing through the motor, and in turn the torque from the previously cited torque-current relationship [38].

Dissipative braking is selected as the braking strategy for E.T.Pack mockup, since it allows for variable torque without the need of battery chargers or controllers, and performs better at low speeds. Power reutilization is not a concern: using the already mentioned speed profile and the motor mechanic power expression, the motor output power is

$$P_{out} = E_{mot} \cdot I_{mot} = \omega_{mot} \cdot T_{mot}$$

It has been computed an expected maximum output power of

$$P_{out,max} = 3.5 \cdot 10^{-3}\text{W}$$

or, numerically integrating P_{out} during the deployment phase, a dissipated energy of

$$E_{out} = \int P_{out} dt = 0.091\text{J}$$

for each deployment manoeuver, which is negligible compared to the on-board battery size (see Section 4.1).
Following the here reported considerations, a DC motor with a planetary gear reduction has been selected from the ones commercially available, such that Equation 3.8 would return a suitable torque for the entire speed spectrum. A MATLAB script has been used to iterate upon different motors and gearbox ratios. Motor model `RS 413-0622` has been eventually picked as the best candidate.

To manage the torque exerted by the DC brake motor during dissipative braking a voltage controller is needed, able to perform PWM control on the motor leads; buck converters are usually used to fulfill such task [39, 40]: in the next Section a DC/DC buck converter is therefore analysed and sized.

3.5.1 DC/DC buck converter design

A DC/DC buck converter has been designed and simulated in MATLAB Simulink to act as torque controller varying the voltage at the leads of a resistor, thus varying the motor output current. The well-known equations for buck sizing have been used [39], that is, named V_i the buck input voltage, V_o the output voltage, L, D, C and R the passive components and δ the duty cycle at a frequency f_{SW}, the relation between voltages is

$$V_o = \delta V_i$$

and the current and voltage ripples as seen by the load are, respectively

$$\Delta I = \frac{V_i}{f_{SW} L} \delta(1 - \delta)$$

$$\Delta V = \frac{\Delta I}{8 f_{SW} C}$$

Since already present on the mockup as later stated in Section 4.1, an Arduino UNO is planned be used to drive the buck converter, therefore the switching frequency f_{SW} must be imposed equal to the one available with the selected microcontroller, i.e. $f_{SW} = 65\text{kHz}$. Noticeably, low switching frequency imply large current and voltage ripples; to limit their maximum amplitude, high capacitance C and impedance L must be selected.
The following commercially available values have been picked and simulated:

$$L = 10\text{mH} \qquad C = 100\text{µF} \qquad R = 20\Omega$$

The behavior of the system has been simulated in MATLAB Simulink via MATLAB built-in electrical simulation toolbox, using a raw PID controller to impose the duty cycle (see the diagram in Figure 3.10). The DC motor characteristics used during the simulation are those of model `RS 413-0622`, reported in Table 3.3.

$k\phi$[V s]	R_{mot}[Ω]	L_{mot}[mH]
0.0139	45.0	1.0

Table 3.3: `RS 413-0622` DC motor relevant characteristics.

A gear reduction between the motor and the reel is imposed, with a gear ratio of $k_{GB} = 1 : 100$. Such reduction is needed since the low speeds of the reel would result in extremely low armature voltages - the maximum reel speed is $w_{reel} = 1.23\text{rad}\,\text{s}^{-1}$, producing an armature voltage of $E = k\phi\omega = 0.017\text{V}$ - making the brake motor useless. In Figure 3.11 the simulation results are reported. It is noticeable how the rise time is not negligible: the target output torque, fixed for the simulation at $T_{ref} = 0.1\text{mN}\,\text{m}$, cannot be reached until a minimum current is produced. Said time can be estimated from equation

$$E_m = R_{tot} I_m \quad \& \quad E_m > 0 \quad \rightarrow \quad E_m - R_{tot} I_m > 0$$

obtained from circuit diagram 3.9b, with R_{tot} the sum of all resistors, which, for non-ideal components, is

$$R_{tot} = R_{mot} + R_L + R_{load} = 45 + 10.85 + 20 = 75.85\Omega$$

with R_L obtained from the inductor datasheet. Motor armature voltage E and current I can then be extracted from

$$E_m = k\phi \cdot \omega_m \qquad T_m = k\phi \cdot I_m$$

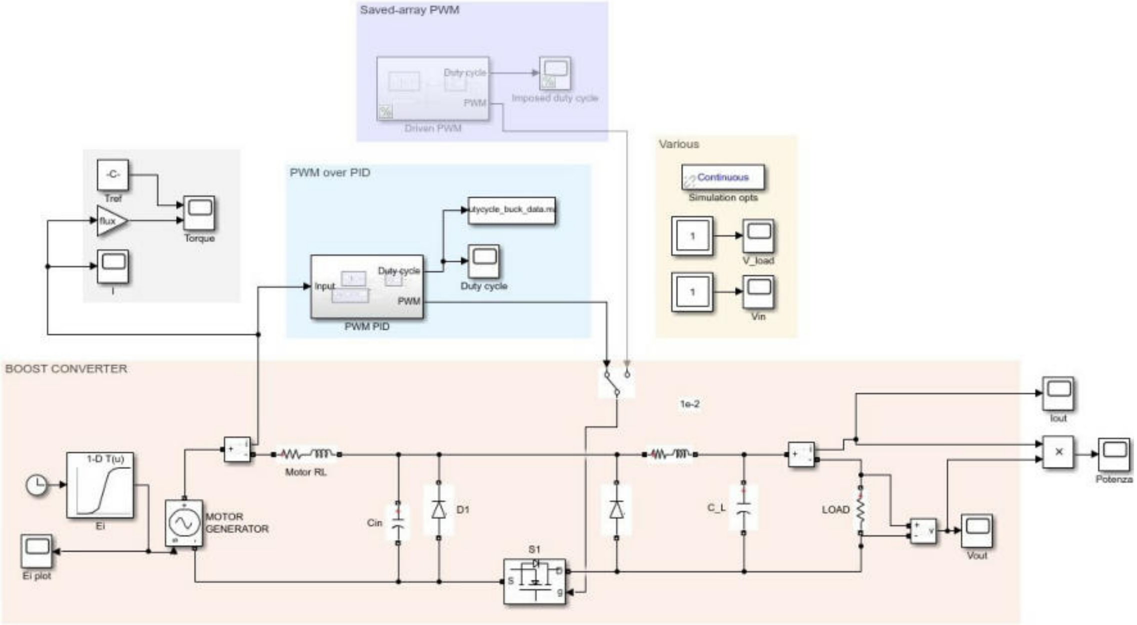

Figure 3.10: Simulink block diagram for the DC/DC buck converter simulation.

resulting in

$$\omega > \frac{R_{tot}T_m}{(k\phi)^2} = 39.26\mathrm{rad\,s^{-1}}$$

For the considered speed profile, the brake reaches $\omega_{brake} = 39.26\mathrm{rad\,s^{-1}}$ - i.e. $\omega_{reel} = 0.393\mathrm{rad\,s^{-1}}$ at the reel due to the 1:100 gear reduction - at time $t = 1.79$s, which is comparable with the rise time of $t = 1.779$s obtained by Simulink's Scope.

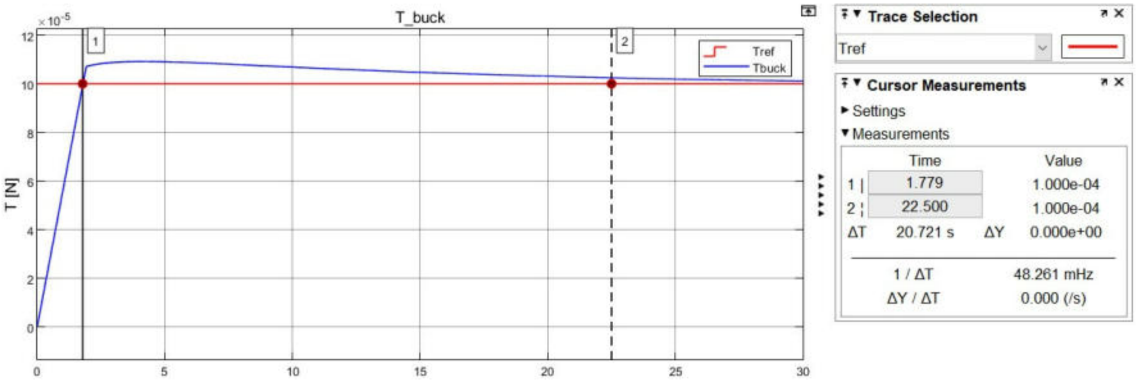

	Time		Value
1	1.779		1.000e-04
2	22.500		1.000e-04
ΔT	20.721 s	ΔY	0.000e+00
	1 / ΔT		48.261 mHz
	ΔY / ΔT		0.000 (/s)

Figure 3.11: Simulink scope view of torque obtained using the simulated buck converter; cursor no. 1 marks the interception point where $\omega_{brake} = \omega_{brake,min}$. The red line is the target torque.

Said time is dependent from the target torque and the acceleration profile: higher torques require higher motor speeds ω_{mot}, thus more time if the same acceleration is considered and, vice versa, lower accelerations result in higher rise times.

The motor torque until here considered is the one only due to its electromagnetic properties. During acceleration or deceleration the motor rotor inertia must also be accounted for; it can be shown that, for a motor with gearbox reduction under acceleration, it is true

$$T_m = k_{GB}T_L + \left(\frac{J_m}{k_{GB}} + k_{GB}J_L\right)\frac{d\omega_L}{dt}$$

which, removing the load torque T_L just for demonstration sake, becomes

$$T_m = \frac{J_m}{k_{GB}}\dot{\omega}_L + k_{GB}J_L\dot{\omega}_L$$

J_m and J_L are the motor core and load inertia respectively; it can be seen how, keeping the load acceleration (i.e. the reel acceleration) $\dot{\omega}_L$ constant, the parasitic torque due to the load inertia J_L decreases with a gear box ratio k_{GB} increase [4] , while the one due to the motor core J_m gets higher.

Therefore, with high transmission ratios such as the one here considered ($k_{GB} = 1 : 100$), the load inertia can be neglected, while the motor inertia must be taken into consideration, since it could add a significant contribution to the total braking torque.

For the selected motor `RS 413-0622`, no rotor inertia was reported by the datasheet; additional tests have been performed in Section 5.1.1 to evaluate how the motor inertia J_m impacts on the total braking torque.

3.5.2 Steppers as brakes

A more unconventional approach concerns the use of a stepper motor being passively driven instead of standard DC motors. The principle of operations is the same as previously reported for DC motors, exception made for the number of phases, which is two for steppers: the rotating magnetic core induces a voltage in the motor coils, which can be exploited to exert a resistive torque. Besides the current-induced torque, steppers also exert a torque due to magnetic interaction of the core permanent magnet with the stator, named *detent torque*, which is non null when the stepper is stationary.

As reported by [41, 42], theoretical methods to predict average and detent torque are available, but require the knowledge of values as the flux linkage, teeth angular position and other, not available in the datasheets of the considered commercial

---

[4] with a gear box ratio increase it is meant that the transmission ratio $1 : X$ is increased, thus effectively decreasing k_{GB} value

products. Empirical torque characterization is therefore needed (cfr. Section 5.1.2). Motor `RS 1805279` is chosen for further testings, being it already available since it was selected to be tested as driver motor and already acquired.
Due to the stepper inner geometry the exerted torque is expected to present a sinusoidal behavior, with a step size of 1.8° as per the motor datasheet. Given the reduction ratio of $1:3$ between the reel and the brake, the step size on the reel side is 0.6°, namely a tape length of

$$L_{tape} = R_{reel} \cdot rad(0.6^{\circ}) = 0.838\text{mm}$$

This is considered an acceptable step size, therefore the incremental motion of steppers is accepted and neglected for this application.

The use of a stepper as brake, unconventional as it may be, simplifies the operations during tape reel-in, as it can be precisely controlled in position and speed without the need of a closed loop feedback as already stated. Therefore, both DC and stepper motors will be tested and their performances evaluated before the final selection for the adoption in the mockup.

3.6 CAD design

The whole E.T.Pack mockup has been designed in CAD (SOLIDWORKS) prior assembly to plan the positioning of each component and verify the fit of pressure lines and electrical routing.
CAD models have also been exploited to realize 3D printed components, resulting in a faster production and overall lighter subassemblies; although dimensional accuracy and mechanical strength of 3D printed PLA are not comparable to those achievable with other production strategies - such as injection molding for plastic and generally metallic components - perfectly operating parts have been achieved and used for the testbed realization. Moreover, intricate geometries such as pockets or hexagonal recesses for easy nuts fastening have been obtained, which are hardly achievable with standard chip removal or non-additive operations.
Figure 3.12 shows the whole CAD model simulating the upper section of the testbed, i.e. E.T.Pack mockup; the four pillars at the bottom provide mechanical interface with the lower SPARTANS translational module.
Due to the metallic base plate of the mockup, repositioning or moving components due to misalignments or wrong positioning is more complex, as drilling new holes is required for every change. 3D printed components have been designed and

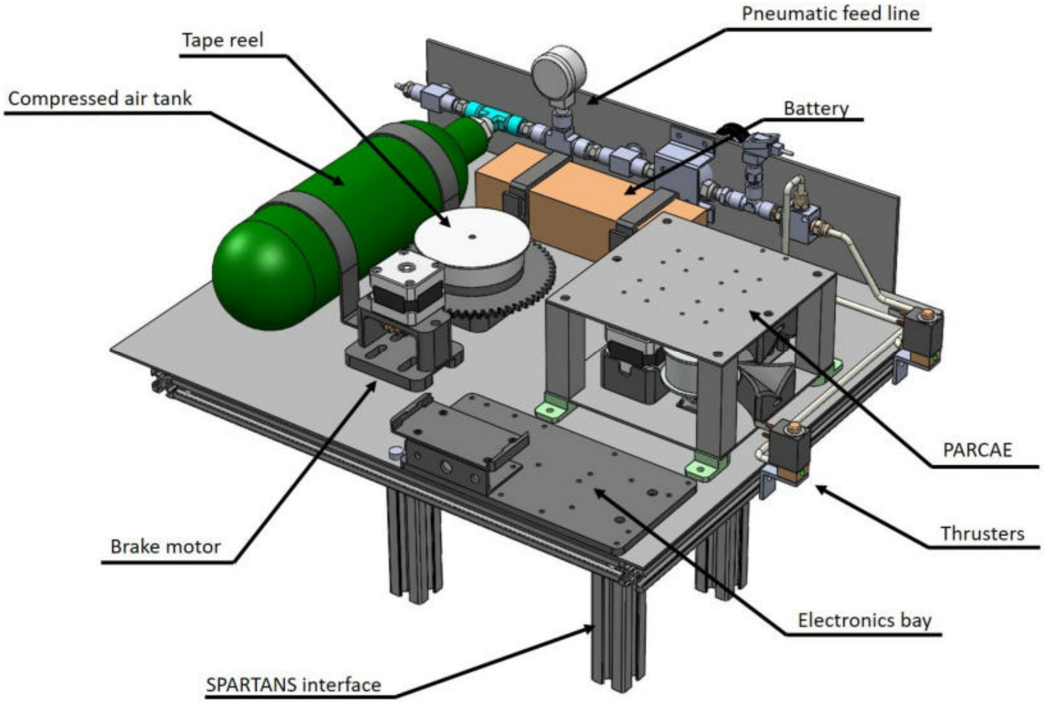

Figure 3.12: CAD model of the mockup, comprising PARCAE, the brake-reel subassembly, the pneumatic line and the mechanical interface with the lower SPARTANS translational module.

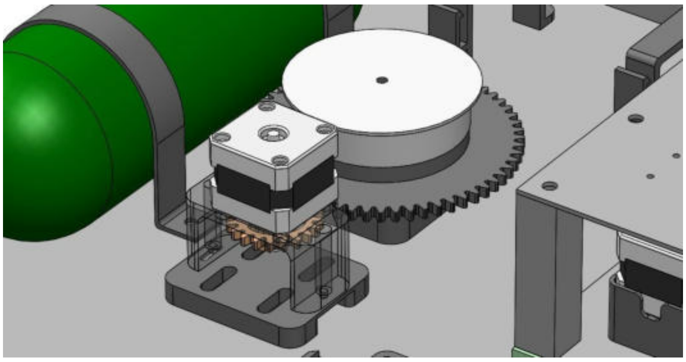

Figure 3.13: Detail of the brake support, which allows for coarse and fine positional adjustments thanks to the built-in sliding features.

built around the concepts of adaptability and possibility of movement in each critical direction, which allows for later adjustments by simply unscrewing the relative threaded fasteners.
In Figure 3.13 an example is reported: the brake motor is mounted on a two parts assembly, of which the flat lower base, interfacing with the metal plate, allows for translation towards and away from the reel gear thanks to the longitudinal slots,

thus adapting for different brake gear size and gear ratios, while the upper C-shaped mount pivots around the right bolt for fine gear meshing adjustment. The gear ratio between the brake motor and the reel has been selected equal to $1:3$ for the current configuration.

Since the motion capture system works in the infrared field, and bare metal is highly reflective to IR radiations, every metallic component has been painted with black mat paint or covered with non reflective tape to minimize its impact on the MC and avoid false readings.

Chapter 4

Communications, software and electronics

Besides the mechanical components, control logic and electronics are needed for proper operations of the system, to ensure a timed tape deployment, commands reception and telemetry exchange. In this Chapter the electronics and the control logic are discussed, followed by an overview of the adopted communication layer and the software, running on both the testbed and on the control stations.

4.1 Electronics and on-board control

Numerous functions are due to be performed aboard the testbed, and the electronic and control subsystem must cope with them, providing a way to remotely and safely control the mockup. The main functions the subsystem will need to provide are:

- Tape deployment, thus powering and controlling the driver stepper motor.
- Braking control and reel-in, by means of the brake motor.
- Pressure measurement of the pneumatic system lines, both for the thrust subsystem and for SPARTANS translation module.
- Thrusters actuation.
- Telemetry and data transmission.
- Emergency shutdown.

4.1.1 Microcontrollers

Control onboard of the testbed is provided by a pair of selected microcontrollers, whose tasks are differentiated and complementary. These are an **Arduino UNO** and a **Wemos D1 Mini**, built upon the ESP8266 chip. They have been picked

for their substantially different features: the UNO provides 13 General Purpose Input/Output (GPIO) pins at a 5 V logic level and 6 analog pins wired to an internal Analog to Digital Converter (ADC) while the Wemos offers a WiFi capable, single threaded chip but less GPIO, at 3.3 V.
The two controllers will manage different aspects of the system; in detail, the Arduino UNO is delegated to controlling the mechanical side of the operations, i.e. the motors and the thrusters actuation, while the Wemos is responsible for data acquisition and transmission, command reception and dispatching and for the emergency shutdown of 12 V rail powering the motors.

Blocking loops and steps timing

The UNO has been chosen to drive the motors both for its higher GPIO count and for the ability to run blocking routines without issues: since pulses timing is critical to faithfully follow the desired speed profile (see below) a dedicated loop is run to prevent other functions from taking up time and slowing the code execution.

```
void deploy() {
  setDriverMotorEnabled(true);

  // [...] code missing

  // this routine is a blocking one (i.e. the loop() is not called)
  // we must manually check for I2C incoming messages, or we could miss some
  // if ABORT_DEPLOYMENT_FLAG is set, stop the motor
  // the flag is set by i2c incoming messages received by checkI2C()
  while (!ABORT_DEPLOYMENT_FLAG && driverStepper.run())
    checkI2C();

  ABORT_DEPLOYMENT_FLAG = false;

  // [...] code missing

  // turn off the motor to prevent driver chip overheating
  // should be turned on if holding torque is needed
  setDriverMotorEnabled(false);
}
```

Listing 4.1: A code snippet from the Ardunio UNO sketch

While the UNO stands long lasting loops in the main routine, the Wemos requires control to be handed to the WiFi and internet manager every 5 s maximum, or the built-in watchdog calls a system reset; being these devices single-threaded, no parallel operations can be run, and the UNO is the sole between the two to allow a 50 s loop - where 50 s is approximately the duration of a deployment manoeuver.
In Listing 4.1 a section of the Arduino UNO code is reported: at lines 10 and 11 is the blocking loop, which apart running the motor only checks for messages on the I2C bus - otherwise stop or control messages would not be received. This ensures a high loop frequency: assuming a motor speed of $3\,\mathrm{rad\,s^{-1}}$, the pulse cadency needed from the microcontroller - one pulse means one motor step - is

$$\frac{n_{pulses}}{\Delta t} = \frac{\Delta\theta}{\Delta t} \cdot \frac{n_{pulses}}{\Delta\theta}$$

where the number of pulses required to drive the motor 1° with $\frac{1}{8}$ microstepping is

$$\frac{n_{pulses}}{\Delta\theta} = \frac{1}{\delta\theta} = \frac{1}{0.225°} = 4.44\text{pulses/deg}$$

in which $\delta\theta = 0.225°$ is the step size. The ratio can be converted to radians as

$$\frac{n_{pulses}}{\Delta\theta} = 4.44\text{pulses/deg} = 254.65\text{pulses/rad}$$

Substituting in the previous equation yields to

$$\frac{n_{pulses}}{\Delta t} = \omega \cdot \frac{n_{pulses}}{\Delta\theta} = 3[\mathrm{rad\,s^{-1}}] \cdot 254.65[\text{pulses/rad}] = 763.94\text{pps}$$

This values translates in a time interval between pulses of

$$\Delta t = \frac{1}{763.94} = 0.00131\text{s} = 1.31\text{ms}$$

which is not excessive, considering the microcontroller clock frequency of 16 MHz. However, allowing other methods to be executed while deploying has shown to take more than 1 ms to complete, hence missing steps and resulting in poor timing performances. The adoption of dedicated blocking loops is therefore advisable.

I2C communication bus

The two microcontrollers must be linked and able to exchange data: since the creation of a I2C bus is needed for other components and already planned (see Section 4.1.3), said protocol has been chosen, this way avoiding having to add a secondary data bus, namely more cables and connections. A brief explanation about the selected protocol is proposed.

I2C (or IIC, Inter Integrated Circuit) is a serial protocol based on the master/slave approach, using a bus of two lines, one for data and one for the clock signal. While there is usually one master on the bus, multiple slaves can be hooked up at the same time, opening the possibility to have a shared two-lines bus that can host hundreds of devices; this is an appealing capability, as the system can be extended and more peripherals added without the need of rerouting barely any connection.

In this protocol, the master IC is the main actor, actively requesting or sending data and imposing the clock frequency, while all slaves respond sending data when asked for. Slaves are identified by a 10-bit address, bringing the admissable total slave count at 1024. [43]

I2C lines need to stay at a defined logic level, which must be shared amongst master and slaves devices. Since the UNO works at 5 V and the Wemos at 3.3 V, a direct connection to the same bus is not feasible. An I2C-safe logic level shifter has been therefore adopted and inserted in the bus; this creates two distinct zones of the serial bus, at 3.3 V and 5 V respectively, which new modules or expansions can be hooked up to. In Figure 4.3 the mockup electronic schematics is reported: the level shifter is clearly visible, connecting pins `SDA` and `SCL` of the Arduino UNO to pins `D1` and `D2` of the Wemos.

It is worth noting that a standard, non I2C-safe level shifter would have not been suitable for the task, as the I2C protocol calls for both lines being pulled high, while common level shifters are usually pulled to ground while not in active use, thus preventing data from being successfully exchanged.

Expandability

Choosing two different microcontrollers for the different tasks (WiFi and telemetry vs. hardware control) leaves the possibility to expand or enhance the system in the future without the need of radical changes to the system. The UNO is a good choice for the current needs, providing enough GPIOs and a sufficient clock frequency, but could become inappropriate in the case more peripherals need to be added, requiring an higher number of digital pins, or if more computational power should be demanded. Replacing the UNO with a more adequate board (like the Arduino MEGA for higher GPIOs count or newer version to increase the computational power) is made easier with such *separation of concerns*, allowing for a wide variety of boards to be installed without the need of it providing a WiFi connection, as said task is accomplished by another controller, but only exposing two I2C bus pins.

As the mockup will be due to revisions and upgrades this is a likely scenario, and therefore the adoption of I2C could be beneficial for future work.

4.1.2 Motor drivers

Two motor are involved in the build - the drive stepper and the braking motor - therefore two motor drivers are adopted; different kinds of controllers are here proposed and discussed for the two different applications.

Driver motor control

For stepper motor `RS 42SH47-4A` - the one driving the pulleys - speed and positioning accuracy are needed and, moreover, said motor can not be driven at the 12 V provided by the testbed power rail, as motivated in Section 3.4.1. A board built around an `A4988` stepper driver chip, offering up to $\frac{1}{16}$ microstepping, thermal protection, current limiting protection, maximum current selection and short circuit protection has been adopted; its output has been constrained at a current $I_{drive} < 1.6$A to respect the nominal current value (cfr. Table 3.1). The board is used in conjunction with Arduino UNO and is therefore 5 V tolerant.

`A4988` requires three inputs to be driven: one for direction, one for enabling and energizing the coils and one to dictate the step sequency. Since most common libraries are based on a four-pin drive pattern[1], or were missing key features related to the particular chip, a new library has been written, based on the already available open-source Arduino Stepper Library [44] and AccelStepper Library [45]. The library accepts rad s^{-1}, rpm and pps (pulse per second) input units and has been provided with convenience methods to control speed, direction, desired rotation count, coils disabling, and more.

The stepper speed has been imposed via a discretization of the simulated speed profile: it has been sampled in MATLAB with 300 points and the corresponding speed and time values have been saved in an array, later imported by the Arduino UNO sketch, which sets the stepper speed according to the elapsed time and the given speed profile. The generated `profile.h` file contains therefore time-speed values couples:

```
uint16_t t[] = {0,        632,      1307,     ...};  // time [ms]
double   w[] = {0.000000, 0.088538, 0.183038, ...};  // speed [rad/s]
```

In Figure 4.1 an example of the discretization is reported, with a lower samples count for visual clarity sake.

Since deployment speed is a key factor, a microstepping value of $\frac{1}{8}$ has been selected,

---

[1] Four pins are usually used to drive steppers using an H-bridge, two pins for each phase

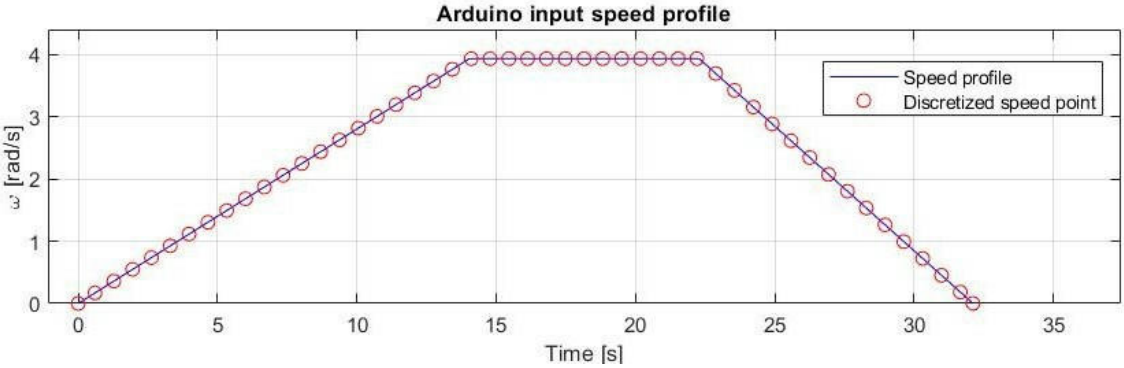

Figure 4.1: Speed profile discretization for generating the input vectors; a smaller samples set is used for clarity sake.

which yields to angular accuracies of

$$\delta\theta = \frac{1}{8} \cdot \frac{360°}{200} = 0.225°$$

while speed accuracy is dictated by the aforementioned time delay between subsequent pulses (cfr. Section 4.1.1). Adherence to the imposed speed profile has been tested and is later reported in Section 5.1.4.

Further key feature is the motor shutdown, since de-energizing the coils while not in use is fundamental to ensure long life to both the battery and the chip itself: neglecting the efficiency and the power consumption of the chip, when energized - i.e. stationary and exerting an holding torque - the stepper consumes a mean power of

$$P = \bar{V}\bar{I} = 2.8[\mathrm{V}] \cdot 1.6[\mathrm{A}] \approx 4.5\mathrm{W}$$

which is not negligible and could, in the long term, shorten the battery life of the mockup. Moreover, the driver board is only passively cooled trough a small aluminum heatsink (visible in Figure 4.2), which gets substantially hot during motor operations; despite the chip offering overheating protection, avoiding high temperatures for long time periods lowers the chances of a chip burnout, which is a known issue for this product.

Brake motor control

As explained in Section 5.1.3, a stepper motor has finally been chosen as the braking motor. During braking operations, the motor leads are shorted to achieve maximum braking torque, as discussed in Section 3.5, and the motor driver is therefore not concerned; during reel-in operations instead, the stepper is actively driven via an `L298` motor driver board, controlled by the Arduino UNO by a custom fork of the

already cited AccelStepper Library.
Since the reel-in speed profile is not a mission requirement, it has been set constant and equal to

$$\omega_{reel-in} = 10\text{rpm}$$

Such low speed eases the rewinding procedures, since tape tangling or being caught inside the pulleys has been observed, and reported in Section 5.1.5. Clearly, said speed is customizable and can be adopted to any operational scenario.
The same considerations as per the `A4988` driver board about overheating and power consumption apply.

4.1.3 ADCs and pressure sensors

Pressure control of the pneumatic lines for both the mockup and the translational module is desired: as far as the mockup is concerned, after a calibration procedure (see. Lungavia, E. [21]) thrust being exerted by the cold gas nozzles can be estimated from the thrusters line pressure value; for the translational module, high-side and low-side pressures are gathered to perform system checks, determine the tanks fill level and to estimate the floating force.
Pressure acquisition is performed by dedicated sensors, namely models CDK `PPE-P10A-H6` for the mockup and SPARTANS low pressure side and model Wika `A-10 0-250bar` for the translation module high pressure side, whose output is a voltage in the range $V_{sens} \in [0; 5]$V (see Table 4.1).

Model	Input pressure	Output voltage
`PPE-P10A-H6`	0 MPa to 1 MPa	1 V to 5 V
`A-10 0-250bar`	0 MPa to 25 MPa	0 V to 5 V

Table 4.1: High and low pressure sensors input/output specifications.

To achieve good reading precisions, a suitable ADC has been used: despite both the UNO and the Wemos having integrated ADCs, they all offer 10-bit resolutions, therefore $2^{10} = 1024$ quantization levels, which correspond to a least significant bit (LSB) voltage of

$$Q = V_{LSB} = \frac{\Delta V}{n_{bits}} = \frac{5}{2^{10}} = 0.00488\text{V}$$

For pressure transducer `A-10 0-250bar` having a $\Delta P = 25\text{MPa}$ input range said LSB voltage translates to a maximum resolution of

$$Q_P = \frac{25}{2^{10}} = 0.0244\text{MPa} = 0.244\text{bar}$$

which is not a satisfactory resolution considering an expected maximum pressure of approximately 80 bar and a working pressure of around 10 bar to 30 bar on that line. Analog to digital conversion via the two ADCs integrated into the microcontrollers is therefore not an option.

External converter Adafruit breakout board 1085 built around the `ADS1115` ADC chip offers instead 16-bit resolution - thus $N = 2^{16} = 65\,536$ quantization levels - and is more suitable to the application: redoing all cited calculation an LSB voltage of

$$Q = 7.63 \cdot 10^{-5}\,\text{V}$$

is found, corresponding to a maximum pressure resolution of

$$Q_P = 3.81 \cdot 10^{-4}\text{MPa} = 3.81\text{mbar}$$

which is considered adequate for the pressure range here concerned.

Other features offered by `ADS1115` are *double-ended/differential reading*, that is, tension measurement relative to an imposed external reference instead of the common ground, built-in programmable gain amplifier (PGA) able to amplifications of up to ×16, four separate inputs and I2C communication with four different selectable addresses. Since two ADCs are needed for the testbed - one for E.T.Pack mockup, one for SPARTANS translation module - they have been connected to the I2C bus with different addressed (`0x48` and `0x49`) to be later distinguishable by I2C master, i.e. the Wemos board.

Aside from having higher resolutions, the adoption of an external ADC allows for the reading of the three pressure values to be executed directly by the Wemos - which has only one ADC integrated channel and could have not handled three inputs - instead of passing through the UNO 6-channels ADC.

4.1.4 Thrust control

Thrust control is achieved by two nozzles provided with electromechanical valves: when fed with a 12 V tension the built-in solenoid opens the pneumatic line, producing thrust. Upon reception of the firing message the valves must therefore be energized. Since neither of the two microcontrollers is 12V capable, a relay has been used to provide the actuation power, hooked up at one side to the control logic, at

the other to the 12V buck converter; it features a protection circuit via an optocoupler to physically decouple high voltages lines from low logic levels one.
Thruster and pneumatic lines design is tackled in-depth in [21].

4.1.5 Power distribution

Power to the whole E.T.Pack mockup is provided by a 6 cells, 22.2 V LiPo battery with a capacity of 5200 mA h, able to sustain active testing on the mockup for different hours. Being the output tension unsuitable for motors or microcontrollers, two DC/DC step-down buck converters have been implemented, one feeding a 12 V regulated bus, the other a 5 V one.

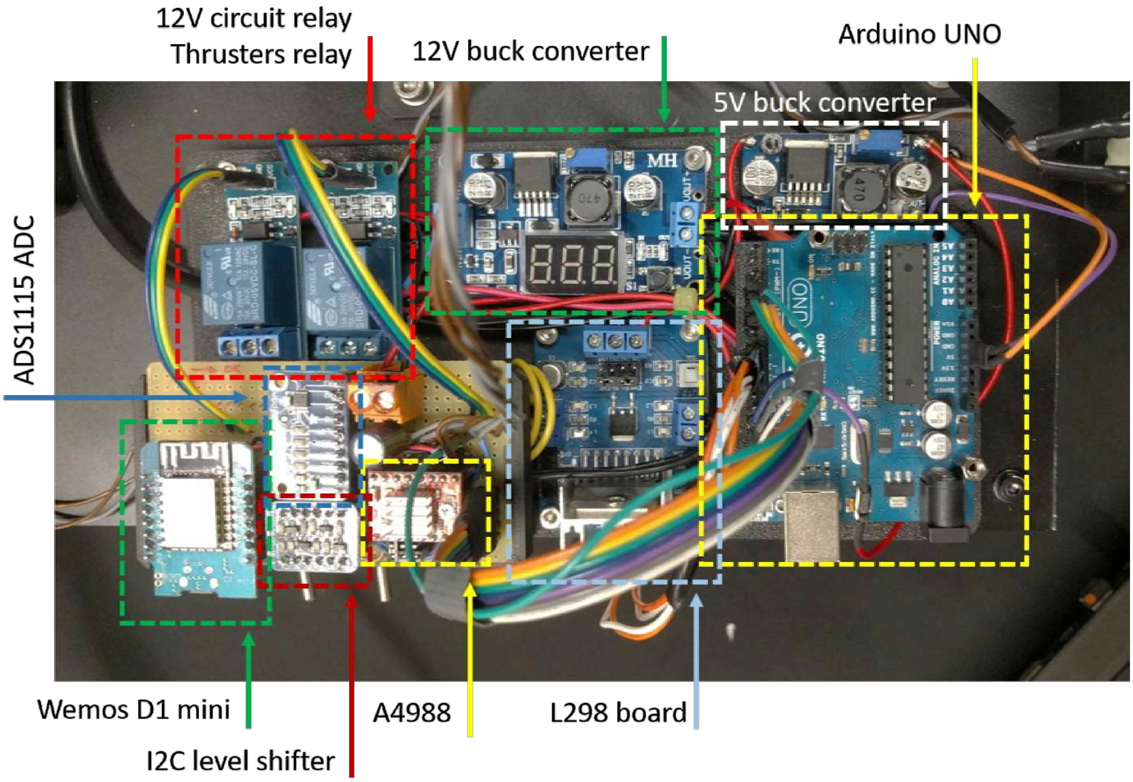

Figure 4.2: Top view of the electronics and control assembly; the main boards and components are highlighted and labeled.

The two bucks are kept separated to enable sectioning of the power distribution subsystem: the 5 V bus is always active, providing power to both microcontrollers, thus keeping an active connection with the base station; the 12 V is instead downstream of a relay actuated by the Wemos, and can be turned on or off remotely. This allows for safety rules to be imposed, as, for example, turning the 12 V rail on

- hence providing power to the motors - only if a connection to the control station is established, or disabling the motors if said connection is lost during a deployment manoeuver.

The battery can be cut off with a physical toggle switch mounted on the side of the testbed, effectively turning off the whole mockup. Said switch is used in cases of emergencies - the mockup not responding to incoming messages - or when not operational. Sectioning and power routing can be observed in the schematic reported in Figure 4.3.

4.1.6 Board design and assembly

Components have been assembled on a custom 3D printed housing and connected with soldered joints or ribbons cables following the planned schematics. For the smaller boards provided with male pin headers (Wemos, I2C level shifter, `A4988` and `ADS1115`) a circuit board has been created with a perfboard (prototyping predrilled sheet with soldering pads underneath) to ease the routing of the numerous needed connections; female headers are used instead of direct solder joints to allow easier maintenance or replacement in case of a failure. An input filtering capacitor ($C = 100\mathrm{m\,F}$) has been used to reduce ripples on the 12V bus due to motor activity. In Figure 4.2 all components are shown and labeled.

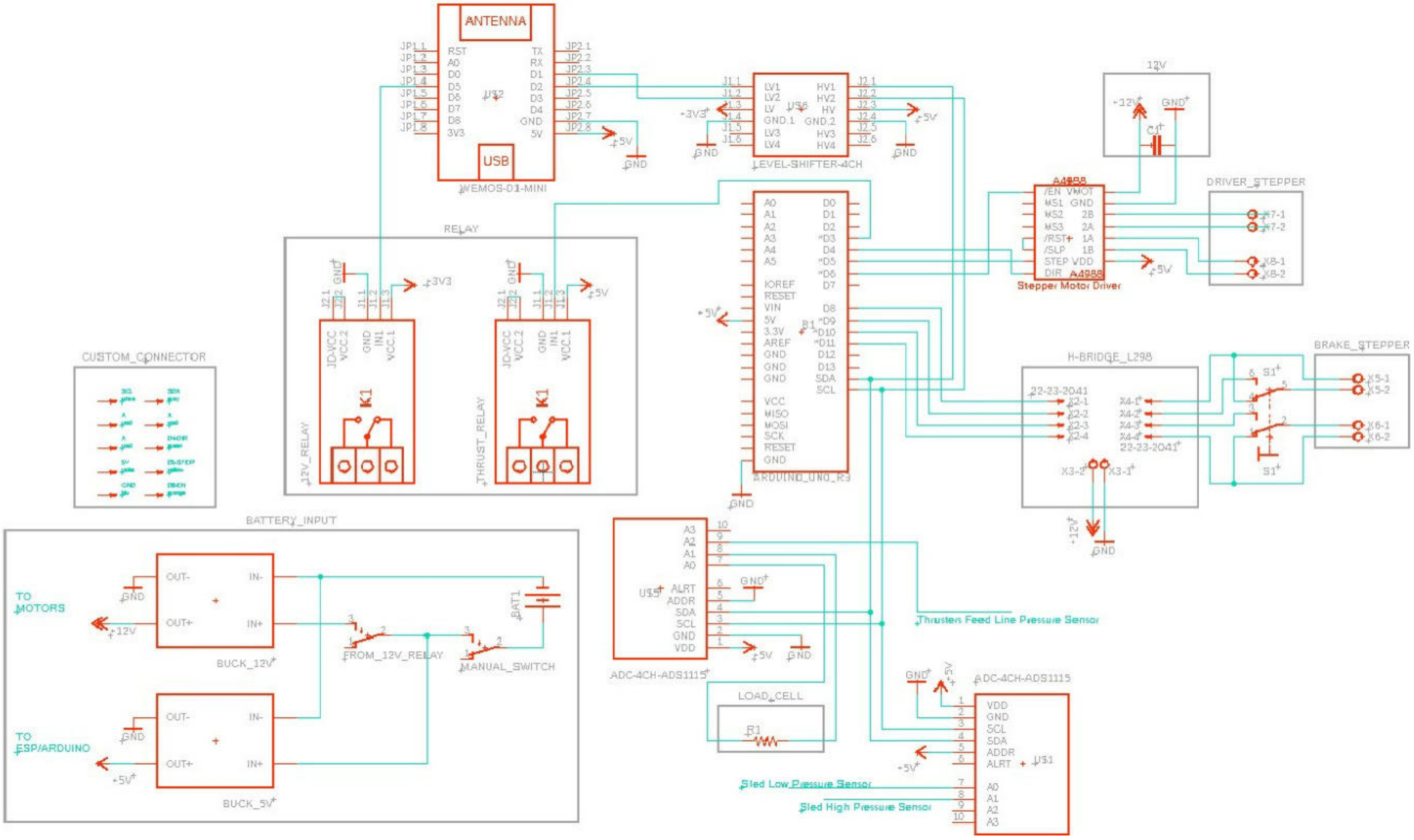

Figure 4.3: E.T.Pack mockup electronics schematics.

4.2 Communication infrastructure

The communication layer must provide fast and reliable data exchange mainly between the testbed and the control station, but expandability is also desired, i.e. multiple devices or peripherals being added without needing to radically modify the software of the existing system. Direct connections controller-to-mockup are therefore excluded. Reliability in dispatching commands is also a must, since it is not tolerable critical messages (as an example, a command imposing to shut down the emergency power switch) are not properly delivered.
Per requirements, moreover, different communication channels are to be used, to dispatch commands, to receive telemetry from the testbed, to read the external load cell tape tension (see Section 4.4). Again, expandability must be an option in case additional sensors requiring a dedicate data channel should be added.
MQTT (Message Queue Telemetry Transport) has been found to offer all required features: it is a standard ISO protocol based upon TCP/IP and organized around a subscribe/publish (pub/sub) pattern; as reported in the official website [46]:

> MQTT is an OASIS standard messaging protocol for the Internet of Things (IoT). It is designed as an extremely lightweight publish/subscribe messaging transport that is ideal for connecting remote devices with a small code footprint and minimal network bandwidth. MQTT today is used in a wide variety of industries, such as automotive, manufacturing, telecommunications, oil and gas, etc.

While offering a virtually infinite number of data channels - named *topics* - and quality of service selection (QoS), which fulfill the previously cited constraints, the library required for its use is extremely lightweight, making it perfect for the usage in embedded systems - or generally devices with restricted capabilities. Moreover, being it a well-known standard, it is available on every major platform - Windows, Mac, Arduino, as well as Android to cite a few - making compatibility not an issue.

4.2.1 MQTT topology and the pub/sub pattern

The architecture of a network using MQTT protocol requires an additional component with respect to a direct peer-to-peer connection; to achieve the pub/sub pattern a central message dispatcher - named *broker* - is needed. Its tasks are to receive all connection requests, assign identifiers and manage the message flow: once a device is connected, it registers on the broker the lists of all the topics it needs to receive messages from - i.e. the *subscriptions* - and, upon reception, the broker forwards the message only if the topic matches one in the provided list. All devices on the network can therefore subscribe to (request messages from) only certain topics, reducing the needed bandwidth and lowering the computational power and execution time used to filter messages onboard each device. Multi-level subscriptions are available via so-called *wildcards* which allow to subscribe to multiple topics simultaneously taking advantage of text-matching rules.

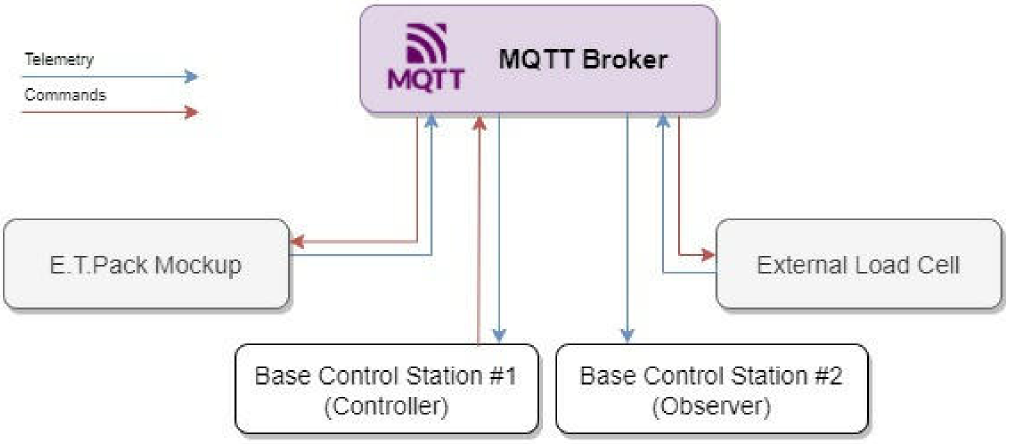

Figure 4.4: E.T.Pack testbed MQTT infrastructure topology.

By exploiting the pub/sub pattern it is possible to plug devices into the network without the need to reroute direct peer-to-peer connections or to alter the source code of any other device. This is particularly useful to allow for different control stations being used during more complex testing campaigns.

MQTT also provides the possibility to define a *last will* message for every distinct connection and the relative last will topic: said message and topic are stored by the broker upon connection and are sent when connection with the device is lost. Last will messages have been used to detect disconnections of the Wemos from the network, enabling the base control to display a warning to the user notifying the unwanted loss of signal.

An illustrative example of the possible network infrastructure is offered in Figure 4.4. Note how routing all connections through a central broker allows for data to be received from all and only from interested devices.

A WiFi router running the open-source firmware OpenWRT [47] has been employed to deploy the WiFi network; being OpenWRT based on Linux, it has been possible to install an MQTT broker directly on the machine, removing the need for additional hardware.

4.2.2 QoS - quality of service

MQTT offers the possibility to choose the quality of the service, namely how each message and its reception confirmation must be treated. The following QoS are available:

- QoS 0: the message is sent but no reception acknowledgment is required; the message could be never dispatched.
- QoS 1: the message is sent, and a reception acknowledgment is required; the message could be dispatched twice or more.
- QoS 2: the message is sent, and a reception acknowledgment is required; the message is assured to be dispatched once and only once.

By imposing QoS 2 on all command messages it is possible to be fairly certain that the command will be dispatched and executed. In addition, it ensures the absence of duplicates - which could lead to errors in the case of time-dependent operations (see Section 4.2.3 for an example).

4.2.3 Telemetry

Telemetry incoming from the mockup is formatted as a JSON object, whose children are the different monitored values - pneumatic lines pressure, motor status, etc. The JSON structure is parsed upon reception by the base control station (cfr. Section 4.3), and eventually by other listeners on the network.
Since various peripherals might send telemetry data, and the microcontrollers used for the task do not usually include a real time clock, but only provide the time elapsed from startup [2], a way to temporally align all incoming messages is needed. All devices has been coded to record the local time at which a SYNC message is received: by using said time as a reference - or *time zero* - for the telemetry all incoming data is in the same time reference system. The SYNC request can be arbitrarily sent by any control station at any given time - usually prior to the beginning of a test session.
The SYNC command is one of the previously cited time-critical cases: if received late or twice, a wrong time reference will be used by that component, shifting the incoming data with respect to the others devices.
Telemetry data rate is imposed at 20 Hz for all devices, but can be scaled up or down depending on the needs and on the frequency of the phenomenon under investigation

---

[2] It is possible to acquire the real time by requesting it to the NTP (Network Time Protocol), but in this case an active internet connection is needed, or by syncing it with the base station via MQTT.

- it should be at least twice the observed frequency as stated by Nyquist-Shannon's theorem, but is usually imposed $f_{sampling} = 10 \cdot f_{phen.}$ for higher accuracy.

4.3 Base Station application

Having an intuitive control station with an immediate user interface has been deemed by the team the best option, rather than relying on third party generic MQTT commercial applications. For ease of integration and data exportation, MATLAB App Designer has resulted the best candidate, as it allows for fast creation of visual apps while still supporting all MATLAB data processing abilities. The base station interface is shown in Figure 4.5: color coded buttons to launch various commands can be distinguished, along with visual status indicators and real time telemetry-driven gauges.

Finename testXX_19082020

App opened @ 19-Aug-2020 11:00:51

Figure 4.5: Control station interface coded via MATLAB App Designer.

The most relevant options implemented by the app are relative to telemetry acquisition and data management. The following options are given:

- Start/stop data acquisition: store incoming values to be later exported or just display the current value.

- Discard previously acquired and stored data.
- Export data by saving it as a `.mat` file for later processing.
- Request SYNC to establish a common time reference system.

Other available options are relative to deployment manoeuver, motor and thruster management and MQTT connectivity. An emergency button is provided to disable the 12V power but in case of an accident.

In a secondary tab - not visible in the reported picture - plots showing the temporal evolution of the incoming values are displayed.

The base station applet joins the MQTT network thanks to the MQTT plugin by the MathWorks Internet of Things Team.

4.4 External load cell

During deployment or reel-in manoeuver, the tape exerts on the external system - i.e. on the vertical post - a force (the tape tension) due to the thrusters being fired or the tape itself being rewound. Knowing the tape tension can be useful during data analysis as it is a good indicator of the deployer status and good working conditions: if spikes or sudden force changes are encountered, it is most likely sign of a failure during the execution of the deployment profile - such as tape slippage, insufficient torque from the driver stepper, loose mechanical components.

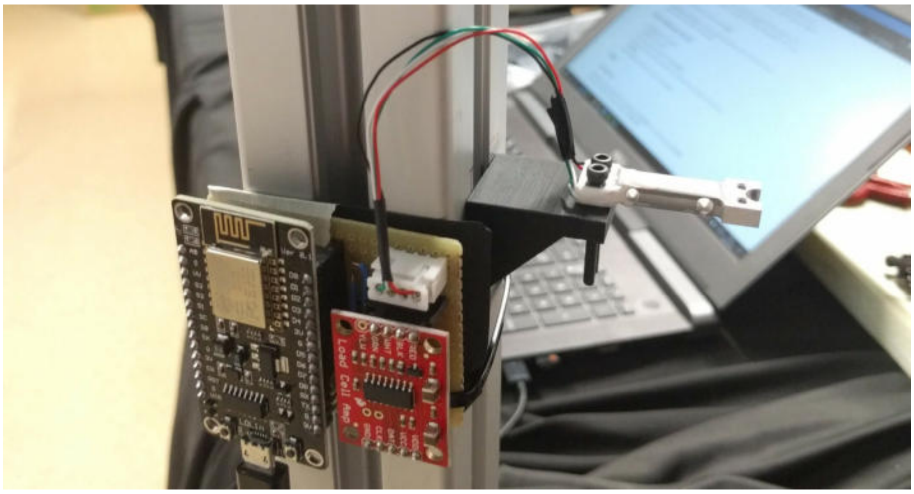

Figure 4.6: The external load cell used to gauge the tape tension, fixed to a vertical post on an angle of the test table, with the control electronics.

Moreover, knowing the intensity of the force exerted by the tape is relevant in case the mass of the host spacecraft is comparable to that of the tape deployer, as this could influence the attitude of the system and the whole tugging manoeuver.

To measure said tension the tape is fixed to a load cell, fixed in turn on a vertical post at the angle of the test table. The load cell has a full-scale maximum value of 100 g, hence allowing for maximum tensions of around 1 N, and is equipped with a full Wheatstone bridge, which provides higher accuracies while cancelling out thermal interferences[3], hence allowing for tension measurements without needing a calibration based on the laboratory thermal conditions. The output tension is read by a precision ADC, `HX711` by Avia Semiconductor, offering differential readings with 24-bit resolution. See Figure 4.6 for a view of the subsystem.

The `HX711` ADC is in turn read by an NodeMCU WiFi enabled development board based on the ESP8266 chip, equivalent to the aforementioned Wemos D1 Mini but with a different size and form factor; measurements are published via MQTT - with a $f_s = 20\text{Hz}$ frequency - and acquired by the control station.

Prior to usage, the load cell has been tested and calibrated; refer to Section 5.3 for the relative discussion.

---

[3] Due to a symmetrical resistance variation in the Wheatstone bridge resistors.

Chapter 5

Subsystem tests

Prior to assembly or during development subsystems and components have been tested, to either quantify their performances, check proper operation or validate the implemented software or hardware solutions. This Chapter focuses on describing the main tests executed and the applied method; minor tests run on hardware or software during development iterations have been here neglected.

5.1 Hardware tests

Hardware and mechanical components, such as the drive and brake motors, have been tested both independently and on a dedicated temporary testbed: a board has been used to fix components relatively to one another and to evaluate different positional arrangements before moving to a stable solution. Adoption of a wooden surface (as in Figure 5.1) allows fast repositioning of the parts using suitable screws without the need of drilling holes for bolts or other fasteners.

As noticeable in the cited picture, a string has been used instead of the aluminum tape. This choice is dictated by the fact that during preliminary system tuning, or if experimenting with different drive speeds or reel height arrangements, the tape would occasionally slide out of the guiding pulleys being mushed into the pulleys flanges or the gears. Being the specific aluminum tape a limited resource and not easily replaceable, a sacrificial medium has been preferred until final tuning, preserving the tape for the proper testing campaign. Electronics and control boards have been wired with jumper cables or in a breadboard; temporary or experimental fixtures have been designed in CAD and 3D printed (visible as the pink components in the image). The here described testbed has been employed for all hardware tests successively reported.

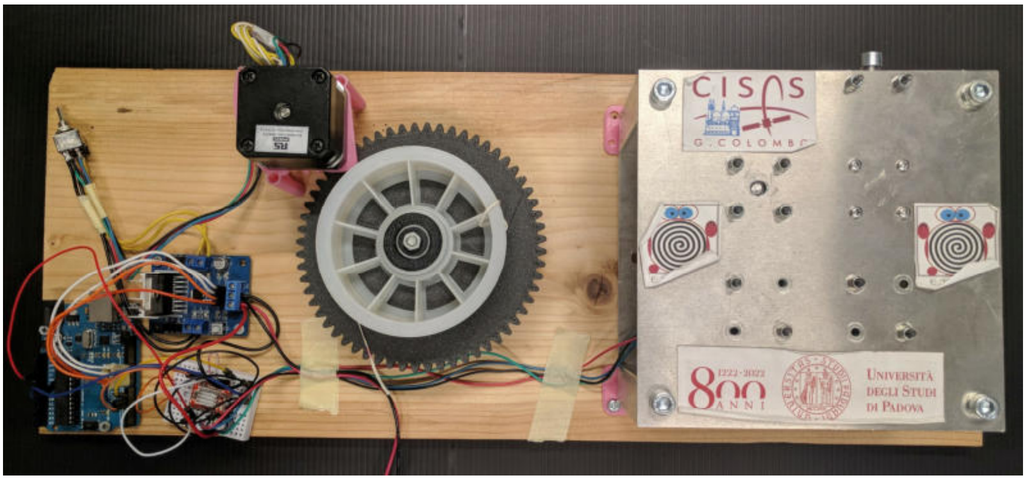

Figure 5.1: Temporary testbed assembled on a wooden board; 3D printed fixtures and components visible in pink PLA plastic.

5.1.1 DC motor static torque

Torque exerted by the selected `RS 413-0622` DC motor with open and shorted leads has been tested to evaluate its adoption as brake motor. The test setup consists of the motor - independent from the whole wooden testbed - coupled with a balanced and symmetric, 10 cm long, 3D printed scale arm mounted on the shaft; the motor has been in turn fixed on an horizontal surface. Known weights have been placed on a tray hung to the horizontally-placed arm, until the arm movement was observed. The procedure has been iterated thrice for each configuration - open or shorted leads.

The mean weight values for which a movement occurs - i.e. for which the exerted torque has been overcome - have been found to be those reported in Table 5.1.

	Open leads	Shortened leads
Weight [g]	76	108
Torque (at brake shaft) [N m]	0.075	0.106

Table 5.1: DC motor static torques with open and shorted leads.

Torque at the reel shaft and the corresponding tape tension have than been computed, the first by means of the known gear ratio between the brake shaft and the reel, the second using the MATLAB script already cited (cfr. Section 3.3). The values found are reported in Table 5.2.

	Open leads	Shortened leads
Torque (at reel shaft) [N m]	0.224	0.318
Tension [N]	2.798	3.974

Table 5.2: DC motor braking torque and tape tension with open and shorted leads.

Following the computed tape tension, `RS 413-0622` DC motor has deemed not suitable for the task, as the resulting tape tension is higher than the maximum acceptable value: if the tape tension generated with open leads had been lower than the maximum admissable one, PWM could have been a suitable option. Since it is higher, torque control is not feasible.

Higher than predicted torques have been observed, and such behavior is charged to the built-in planetary gear reduction exerting friction and parasitic forces and to the motor core inertia, as discussed in Section 3.5.1.

The motor under discussion will therefore not be used as the main braking option, but further testings are desirable - with other motor and gear box combinations - as DC motors present good braking characteristics as earlier discussed (cfr. Section 3.5).

5.1.2 Stepper brake torque

Evaluation of the braking torque realized by `RS 1805279` stepper motor with open or closed leads follows the same procedure as reported for the DC motor, with the only difference being the scale attachment: a pulley with radius $R_p = 20\,\mathrm{mm}$ was used, since a lower torque was expected and shorter levers results in higher force - considering the same torque - hence higher accuracy is achievable with the calibrated weights. Obtained torque and tension values are reported in Table 5.3.

It can be noted, with reference to Section 3.5.2, that the main contribution is given by the detent torque, providing about $5\,\mathrm{mN\,m}$ with open leads.

Being the selected motor a stepper with the nominal tension equal to the power bus one ($12\,\mathrm{V}$), an H-bridge will be used to drive it; during reel-in or driven operations, the motor will be powered by its driver board, while during braking (i.e. with the H-bridge de-energized) its leads will be shortened by a dedicated physical switch. In this way, the current produced by the motor's coils will be dissipated in the circuit with the least electrical resistance, i.e. the coils proper one. Since the obtained tape tension values are in the desired range, the stepper has been declared appropriate

	Open leads	Shortened leads
Weight [g]	26	37
Torque (at brake shaft) [mN m]	5.101	7.259
Torque (at reel shaft) [mN m]	15.304	21.778
Tension [N]	0.193	0.274

Table 5.3: Stepper motor braking torque and tape tension with open and shorted leads.

and will be assembled in the final mockup configuration.
As discussed, the adoption of a stepper as brake simplifies reel-in procedures thanks to the intrinsic accurate open loop positioning and speed control.

5.1.3 Drive stepper selection

As reported in Table 3.2, two steppers have been selected to be evaluated and compared. To test the exerted torque and their ability to drive the pulleys assembly without issues, each motor has been in turn mounted in the temporary test setup with a proper 3D printed adapter and run with different testing conditions; the motors have been subject to: a) numerous speed profiles, with hard and soft accelerations; b) high and low pulleys preloading forces, i.e. variable tightness of the preloading bolts; c) different braking torques.
All applied testing conditions fall withing actual or expected working ranges, with an incremental factor of about 15% for acceleration and speed values. `RS 1805279` motor has been tested while driven by both an `L298` H-bridge board and by the `A4988` driver, being it suitable for 12 V direct feeding, while `RS 42SH47-4A` has only used in conjunction with the cited `A4988` chopper driver.
While both motors do perform correctly under normal circumstance, for high preloading and hard acceleration combinations it has been observed stepper motor `RS 1805279`, which provides a torque of $T \in [0.10; 0.13]\mathrm{N}$ for the considered speeds as per its datasheet, occasionally loosing steps, specifically while at high speeds during the last phases of the initial acceleration. Although this happens only in abnormal circumstances, said stepper has been discarded as driver motor, both for precaution and to keep wide operational margins in case higher speeds or torque values should be requested, even for future applications of the testbed. `RS 42SH47-4A`

stepper motor has therefore been selected as the definitive PARCAE driver.

5.1.4 Stepper deployment accuracy

Ability of the stepper motor to faithfully replicate the imposed deployment profile has been tested, both to to verify the correct implementation of the modified stepper library and to ensure proper working of the `A4988` at a $\frac{1}{8}$ microstepping resolution.

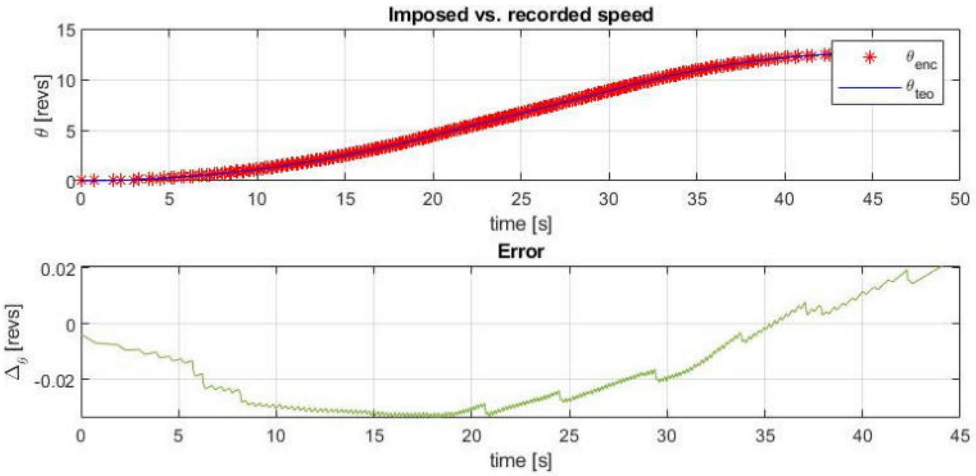

Figure 5.2: Evaluation of the stepper speed and position profile by means of a rotary encoder; red point are the empirical values, the underlying blue line the expected deployment profile.

Speed acquisition has been performed via a rotary encoder fixed to the motor shaft by means of a 3D printed adapter. Results are reported in Figure 5.2: over a 45 s long deployment manoeuver the accumulated error in terms of the shaft angular position has been measured to be 0.02 rev, or 0.1257 rad; this in turn corresponds to a tape length variation from the foreseen one of $\Delta L = \Delta\theta \cdot R_{pulley} = 3.14\,\text{mm}$. Although not being an outstanding result for a stepper motor with $\frac{1}{8}$ microstepping, the deviation from the planned profile is not excessive and acceptable for the application.

An observation is due regarding the test reliability: the used rotary encoder is not a precision metrological tool, offering only 32 steps per turn, and neither is the acquisition board - an Arduino Mega. Positioning reading do reveal, in fact, sharp variations in some cases, which is deemed to be due to the low quality of the acquisition system. Real performances are believed to be better that measured, but this remains an assumption and not better experimentally quantifiable; the test is anyhow reported for completeness.

5.1.5 System tests and assembly

Once completed the final components selection a full hardware check has been conducted, testing for nominal operation of all selected components in their final configuration, and running the first preliminary tests of the completed assembly. Deployment manoeuver and reel-in procedures have been run - without and subsequently with tether - looking for tape slippage or tangling, driver motor and brake torque adequacy, deployment software routines correctness and overall good functioning.

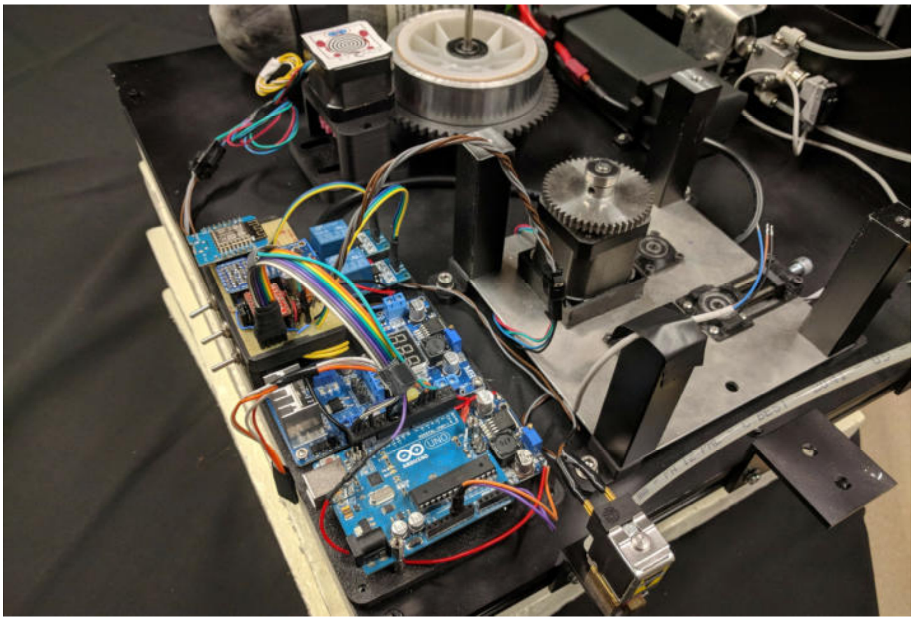

Figure 5.3: The mockup during final assembly; the exterior metal surfaces are painted black to reduce interference with the MC system.

Since no major issue had been found, and being the minor one - predominantly software wise - addressed and fixed, the system has been moved onto the metal frame for the manufacturing of the definitive configuration. In Figure 5.3 the mockup is reported during assembly of PARCAE subsystem: the drive stepper motor is visible already mounted inside the chassis, with the three pulleys and the meshing gears missing. The final mockup configuration has been tested as well, as already cited: during reel-in operations testing, problems with the tape being mushed by the pulleys have been noticed, due to the absence of a guiding pulley. While during reel-out the tape is guided by a freely rotating pulley into the two actively driven ones, thus being correctly routed along the vertical direction, during reel-in the tape directly encounters the driven pulleys, and if its direction is not aligned and in-plane with

them it gets damaged and eventually cut by the flanges. To address the issue two guiding convex surfaces - visible on the exit side of PARCAE in Figure 3.12 - has ben cadded and printed. Their shape guides the tape to the correct height, thus eliminating the problem.
Since hardware integrity and proper operations had been assured, communication and telemetry tests have been consequently executed.

5.2 Communication infrastructure

The communication and telemetry layer has been subjected to thorough testing to ensure no experimental data nor control is lost during the testing campaign. The subsystems composing the whole infrastructure have firstly been isolated or tested independently to exclude the contribution of other factors, and finally the whole system has been tested at once.
Communication from the base station to the mockup has been verified with the testbed logging the received messages to an external display, and its ability to reconnect after a connection lost by cutting the WiFi signal on purpose; reacquisition of the link with the WiFi router has been measured to occur 2 s to 5 s after reestablishment of the WiFi network.
Telemetry transmission from the mockup to two base stations active at the same time has been proven as well, firstly by generating known steady values onboard of the Wemos and matching them with the received and displayed ones, secondly by dry running a deployment profile - without tape - and checking the received status values. Pressure transducers have not been calibrated or tested since their calibration is performed in factory; only a qualitative evaluation of the pressure profile variation has been performed, checking if the time evolution corresponded to the expected one following manual variations on the pressure feed line - opening and closing valves, discharging the pressure line via the thrusters. Plots and virtual gauges of the control station interface has been verified with the same procedure.
Data acquisition and exportation was showcased by running a known profile and exerting a steady force on the load cell by means of known weights; the time sequence and the exported values of the test, opened in a MATLAB script, have been compared and matched with the expected ones, highlighting no issues.
The 12 V emergency switch responsiveness has been measured to under 500 ms during normal operations, likewise the reaction to every other incoming MQTT command, showing the ability to safely shut down the motors in cases of potential threat to the safety of the system - mockup too close to the table edge, tape tangling or being mushed by the gears, etc. Onboard safety routines have been coded as well,

implementing watchdogs to cut the motor power following planned events, such a connection lost or exceeding of telemetry thresholds. Such routines have been subsequently removed for the testing campaign as manned operations have shown to be sufficient to guarantee a safe mockup utilization.

5.3 Load cell

The external load cell used to measure the tape tension exerted on the post needs calibration and testing prior to usage. The Wheatstone bridge differential voltage read by the acquisition board `HX711` is output as a raw reading value of 24 bit; conversion to voltage is not performed since the only relevant value is the force, and mapping of raw values to weight is possible, removing the need for an additional - and potentially error-inducing - unit conversion.

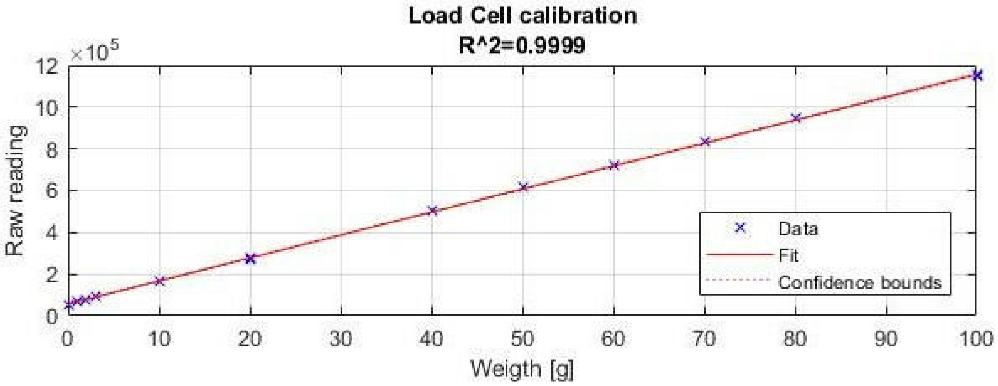

Figure 5.4: Load cell first order calibration curve, presenting narrow confidence bounds and a good coefficient of determination ($R^2 = 0.9999$.)

Calibration has been performed via known precision weights (class M3 with maximum error of $\epsilon = \pm 500\,\text{mg}$) being posed onto a tray hung from the load cell; 25 readings have been gathered in sparse order, with weights in the range from 0 g (unloaded) to 100 g (full scale). A settling time has been allowed to the system to achieve stabilization of the reading and dampening of the tray oscillations.

To obtain the calibration curve a first order linear fit has been computed in MATLAB, reported in Figure 5.4. The resulting curve is satisfactory, with good linearity from the load cell response and a coefficient of determination $R^2 = 0.9999$, indicating low variability in the response of the system.

A small offset error is observed and probably attributable to the load cell own mass; a linear model with both the regression coefficient - or line slope - and the offset has been implemented onboard of the NodeMCU responsible for the load cell data acquisition, enabling it to transmit already converted force values instead of the raw reading. This allows to directly read the measured value on every network client, without the need to implement the mapping function on each; in this way, a few MCU cycles are lost and traded for convenience - although a minor impact on the processor is expected, being the mapping function a simple linear model.

Both the mapped force value and the raw reading are transmitted via telemetry for redundancy.

A remote tare option has been included in the base station app to tare the scale prior to each testing run, effectively setting the offset value to the current reading. This allows to have a calibrated zero removing possible imperfections in the load cell orientation, which could cause small increments in the output due to the cell own weight.

Chapter 6

Experimental campaign

Following the mockup design, realization and testing the first experimental campaign was conducted and the already mentioned tests performed (see Section 2.4). This Chapter focuses on describing the test procedure and the obtained results, followed by a brief analysis of the impact of the here mentioned findings. The tests here cited are also reported by Olivieri, L. et al. [48].

6.1 Experimental setup

The test setup consists in what already described in Chapter 2: a 3 m × 2 m glass table providing interface with SPARTANS low friction module, on top of which E.T.Pack mockup is mounted. The movement of the system is acquired by SPARTANS motion capture system (MC), while tape tension between the module and the post is measured by the cited load cell. The system has therefore 3 degrees of freedoms.

In Figure 6.1 the system ready for testing is depicted: the tape is fixed to the load cell at the post, slightly tensioned, and the testbed stands near the corner, aiming at the opposite one; moreover, two fiducial IR markers are clearly visible standing out from the black background. A total of five markers has been used, four on the mockup - with three being the minimum number for a correct trajectory reconstruction, and the fourth for redundancy - and one on top of the post, used for sanity checks - monitoring absence of measurements shifts - and to define the origin of the reference system.

During tests a team of minimum three staff members were present to accomplish all required tasks: a) control and manage MC calibration and startup sequence, as well as starting and stopping data acquisition, from the relative PC; b) remote control of the test sequence from one of the base stations, sending thrust or deploy orders and

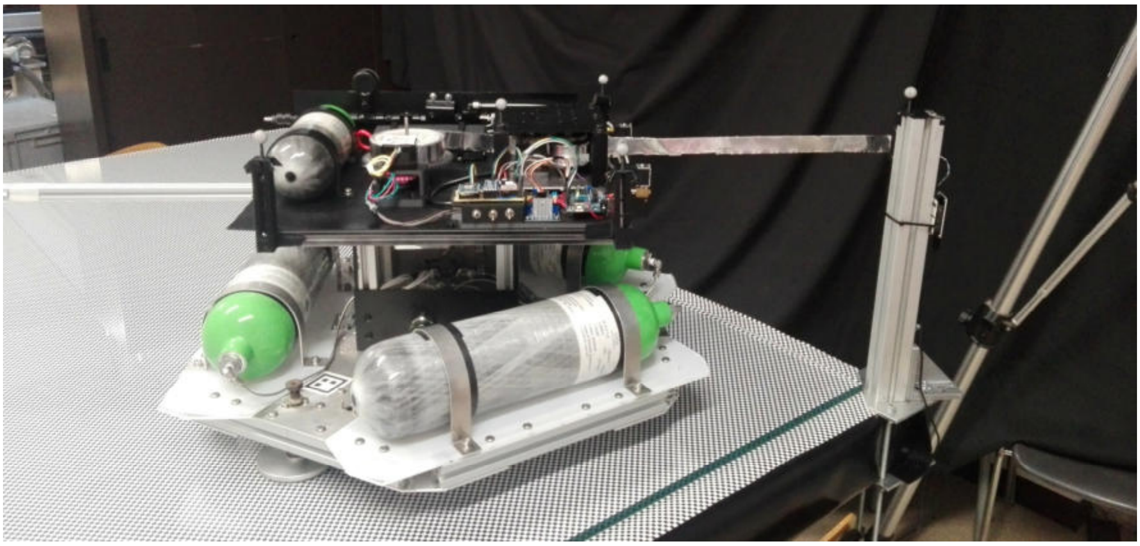

Figure 6.1: E.T.Pack mockup on the glass table prior a testing campaign; the tape is tense and fixed to the load cell at the edge post.

monitoring pressure and tension values, remote shutoff if needed; c) direct control of the testbed by opening the valves of the floating system and the feed lines for the actuation thrusters, as well as assuring manned control over the system physically blocking or turning it off in case of a safety hazard.

Test procedures are at the moment not automated, i.e. each phase of the testing sequence must be manually launched from the control board (see Section 6.4 for an example of testing sequence); scheduled sequences are being evaluated, but the ability to control each phase independently allows more granular control over the whole test. As an example, independently controlling thrusters and the deployer motor gives the operator the possibility to wait for the oscillations following the first thrusters firing to dampen out and for the tape tension to become constant before proceeding.

6.2 Thrusters authority

The test aims at determining the correlation between thrusters feed line static pressure and produced thrust force, and is described and analysed by Lungavia, E. [21]. The findings are here briefly reported.

As in Figure 6.2, a linear correlation between the thrusters static pressure and the exerted force has been observed, with a good coefficient of determination of $R^2 = 0.9997$. Such linearity allows for and easily predictable and controllable thrust exertion.

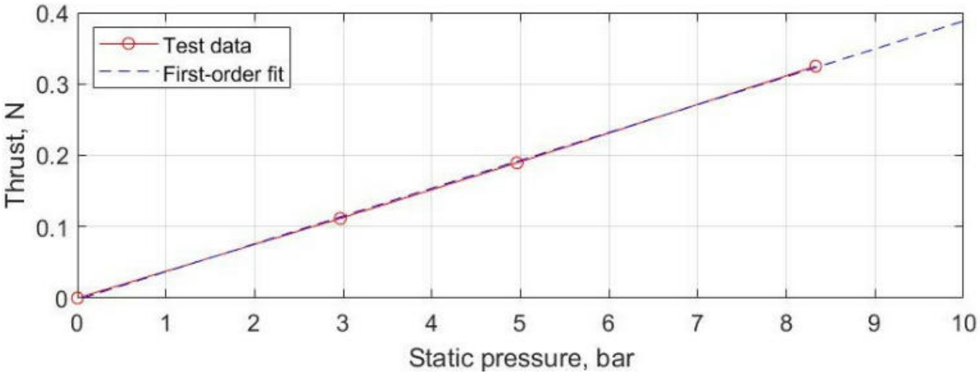

Figure 6.2: Relation between produced thrust and static feed pressure; measured correlation (red) and linear fit (dashed blue) are reported; good linearity ($R^2 = 0.9997$) is achieved.

6.3 Tape viscoelastic properties

By applying a constant tape tension via the onboard thrusters, stiffness k and damping c of the aluminum tape, or more generically of a flexible line, can be computed. An in-depth overview regarding the test and the obtained results is given in [48]. A good match between theoretical and experimental data has been obtained for both a polyamide line - a fishing line - and for the aluminum tape.

6.4 Deployment manoeuver

Deployment and reel-in procedures have been tested both to demonstrate the capabilities of the system to perform and simulate such tasks and to verify the correctness of the deployment profile, in terms of deployment speed and deployed tape length, by comparing the translation acquired with the MC system with the predicted and imposed one. The following Section focuses only on the deployment one.

6.4.1 Test sequence

The test has been set up as previously reported, with a three-men team overlooking the execution. The mockup is positioned at a corner of the table, aiming for the opposite one; this gives a total of 3.6 m of available test space. The imposed speed deployment profile consists of:

a) constant acceleration $a_1 = 0.007\,\mathrm{m\,s^{-2}}$ for 0.7 m
b) coasting ($a_2 = 0\,\mathrm{m\,s^{-2}}$) for 0.8 m

c) constant deceleration $a_3 = -0.01\mathrm{m\,s^{-2}}$ for 0.5 m

as already reported and visible in Figure 3.3.
The scheduled events sequence for the reel-out test, after testbed and facility checks and setup, is as follows:

1. Mockup power on: the testbed is leaning on the table, connected and ready to accept commands.
2. SPARTANS floating module valve opening; the testbed is now freely floating.
3. MC data and testbed and load cell telemetry acquisition start; SYNC request.
4. Mockup 12 V rail power on: the testbed is now able to move the motors.
5. Thrusters firing; the testbed is now exerting force and tensioning the tape.
6. When stable, deployment start: the testbed starts releasing the tape.
7. After about 45 s the profile completes: the testbed is now steady and exerting force onto the tape.
8. Thrusters off: the testbed is now steady and free floating.
9. MC and telemetry acquisition stop.
10. SPARTANS floating module valve shutoff: the testbed is not leaning.
11. Mockup power off.

During the test, the execution has been nominal until sequence point num. 6: after about 15 s from the deployment command a rotation about the reel axis was observed, implying the mockup changing direction towards the table border. At time 25 s from deployment start the execution was halted for precaution, since the undertaken direction could have lead the mockup too close to the glass surface borders. While the full sequence was not tested, more than half of the predicted profile was successfully executed.

6.4.2 Results analysis

The combined results from the MC system and the telemetry have then been elaborated in MATLAB; in Figure 6.5 the reconstructed 2D trajectory as well as the deployed tape length and deployment rate are reported.
The reconstruction shows good accuracy in replicating the imposed profile, both in terms of length and deployment rate, demonstrating the ability of the mockup to simulate accelerations and coasting phases. As shown in Figure 6.3, a drift from the imposed position is observed, peaking at approximately 8 cm at cutoff ($T = 24$s); this behavior has been traced back to low pressure in the floaters subsystem, leading to increased friction and, ultimately, to the inability of the testbed to keep up with the desired profile. This observation is corroborated by the test footage (see

Figure 6.4, more clearly visible in snapshots 4 to 6) where the tape is seen not tensioned, bowing and twisting, indicating the mockup struggling in keeping the deployment pace. In the same way we explain the speed offset, on average null until the 10 s mark, then peaking at $-2\,\mathrm{cm\,s^{-1}}$ at 15 s and maintaining a negative shift; in fact, computing the mean speed deviation yields to $L'_{avg} = -0.33\mathrm{cm\,s^{-1}}$, which corresponds to a traveled length of -7.8 cm over the 24 s manoeuver, in agreement with the observed ΔL shift. Fluctuations and spikes in the speed profile are instead due to the calculation procedures, which infer the mockup translation speed via the finite difference method:

$$L' = \frac{|\vec{p}(t+dt) - \vec{p}(t)|}{(t+dt)-t}$$

where $\vec{p}$ indicates the mockup position in the 2D reference plane.

Smoothing can be achieved by employing a low-pass filter on the speed signal; in Figure 6.3, the blue dotted line represents such signal filtered at $f_{cut} = 1\mathrm{Hz}$.

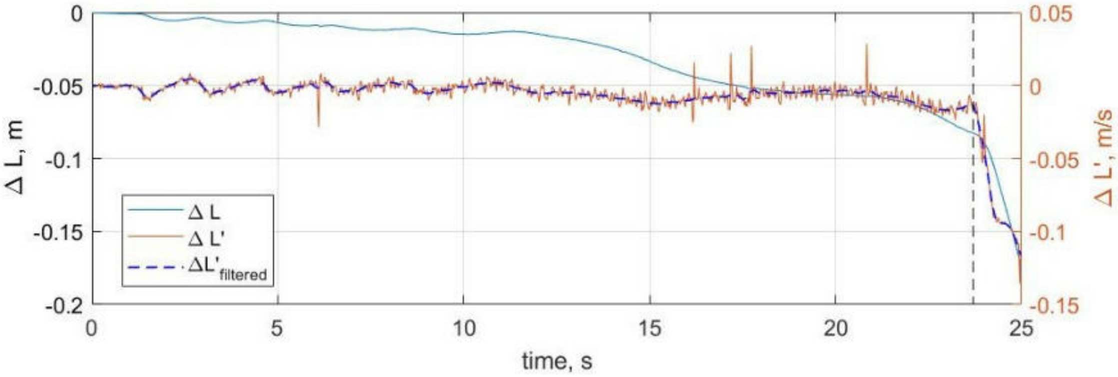

Figure 6.3: Position and speed deviations of the mockup from the imposed target profile as measured by the MC system. The speed signal has beed filtered with a cutoff frequency of $f_{cut} = 1\mathrm{Hz}$.

As mentioned, a rotation of the mockup body is observed; this is deemed to be due to conservation of angular momentum: the tape reel, acting similarly to a reaction wheel, is spun up during reel-out; as the system must preserve its initial angular momentum, an opposite rotation is expected, whose amplitude is dictated by the total momentum balance, as below reported:

$$H_{sys} = I_{reel}\omega_{reel} + I_{body}\omega_{body}$$

Being $H_{sys} = 0$ since the mockup is initially stationary, and neglecting the friction with the table - conservation of angular momentum is valid if no external torques are acting, or must otherwise accounted for - yields to

$$\omega_{body} = -\omega_{reel}\frac{I_{reel}}{I_{body}}$$

The rotation rate is expected to decrease during deceleration, since ω_{reel} gets lower, but has not been observed due to the early test termination.
It can be noted how it is possible to prevent such behavior with active attitude control, by firing the thrusters independently and thus exerting and controlling torque other than force, or by positioning the thrusters asymmetrically so that the generated torque counteracts to the conservation of angular momentum.
In addition the the conservation of the angular momentum, the torque could be a priori attributed to an asymmetric placement of the thruster nozzles or to an unbalanced thrust. This scenario has however been neglected, since a calibration of the thrust subsystem had been run prior the experimental campaign by verifying that the testbed would follow a linear trajectory when left free floating under the sole action of the thrusters. The table had been carefully leveled as well.

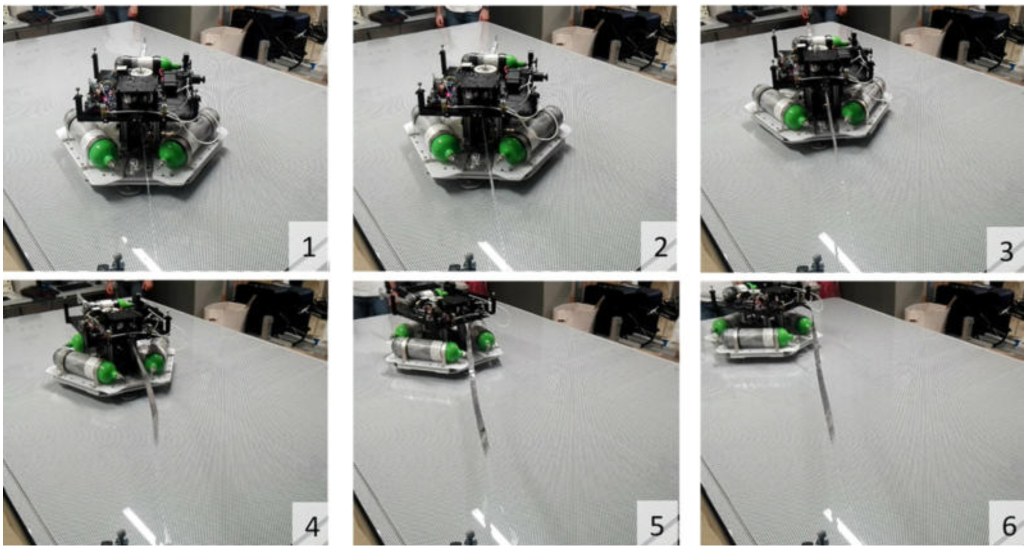

Figure 6.4: Frames captured by the deployment test video; note how the tape bows and twists in frames 4, 5 & 6 due to insufficient tension.

Although the testing conditions are not representative of the predicted flight deployment profile - lasting up to 1 h as in [27], while expected to last from 30 s to 50 s depending on the profile during the experimental campaign - and despite the mockup offering only 3 degrees of freedom out of 6, the test is valuable for the ongoing E.T.Pack design: validity of the rotating reel design has been proven as a solid tether deployment concept, and moreover good performances have been observed, with the tape not tangling nor twisting once exited the mockup thanks to the initial linear momentum imposed by the thrusters.
Additionally, a strong interaction of the thrusters ejecta with the deployed tape has

been noted, with the compressed air interacting with and stressing the aluminum foil if not kept tense, which was not expected to be so noticeable; further considerations are being made by E.T.Pack team regarding the phenomenon and the position of the thrusters relative to the tape exit location.

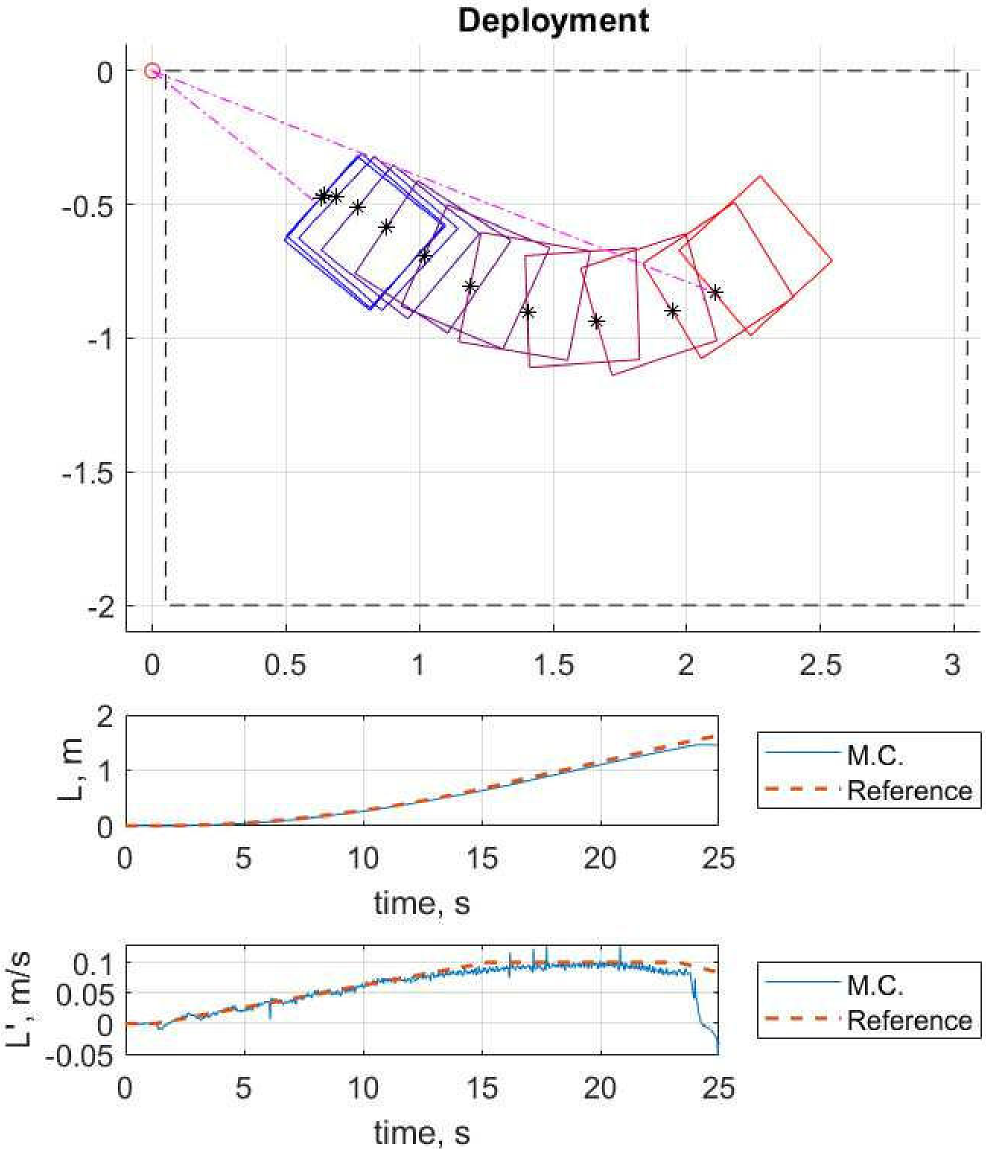

Figure 6.5: Mockup position reconstructed by MC data during deployment manoeuver: 2D module position on the test table (top), deployed length (middle) and deployment rate (bottom).

6.5 Reel-in capabilities demo

As a secondary objective of the mockup, reel-in operations have been tested only to showcase the capabilities of the system, while at the moment not serving the most relevant to E.T.Pack Team, being the aim of the project the sole deployment of the tape.

6.5.1 Test sequence

The test setup retraces what already reported, with the only difference being in the initial state of the system and the reel-in speed profile. The mockup has been initially posed at about 2.5 m from the corner which the tape is fixed at, and the same acquisition and test startup procedure has been run. The speed imposed to the brake/reel-in stepper motor is constant and equal to 8 rpm which, accounting for a gear ratio between the motor and the reel of 1 : 3 and the reel radius of 0.08 m, results in a tape deployment speed of about $0.02\,\mathrm{m\,s^{-1}}$.
After stabilization of SPARTANS floating module the thruster firing and subsequently the reel-in commands have been sent; after an initial acceleration phase followed by an oscillation induced by the mockup inertia, the steady speed rewinding operation was fully performed, with a total time of 92 s, longer than the previous one because of the lower reel speed. The test was halted with the mockup at about 0.7 m from the reference corner, after the rewinding of a tape length of 1.84 m.

6.5.2 Results analysis

From both direct observation and after processing the acquired data in MATLAB, it can be stated that a complete reel-in operation was successfully performed.
Figure 6.6 shows the deviation of the measured velocity of the mockup from the imposed - constant - profile of approximately $0.02\,\mathrm{m\,s^{-1}}$: after the initial low-frequency oscillation of the system due to the mockup high inertia has been dampened, at about 20 s from the beginning of the operation, a quasi-steady reel-in profile is obtained, fluctuating around a null delta value. Again, the high-frequency spikes are attributed to the MC noise coupled with the finite difference method employed for the speed computation.
Referring then to Figure 6.8, it can be stated that a quasi-linear trajectory has been reconstructed, with a less marked rotation.

Similarly to what noted in the deployment test, a rotation of the body due to conservation of angular momentum can be observed both in the reconstructed data and in the video stills, with in this case the additional presence of a restoring torque

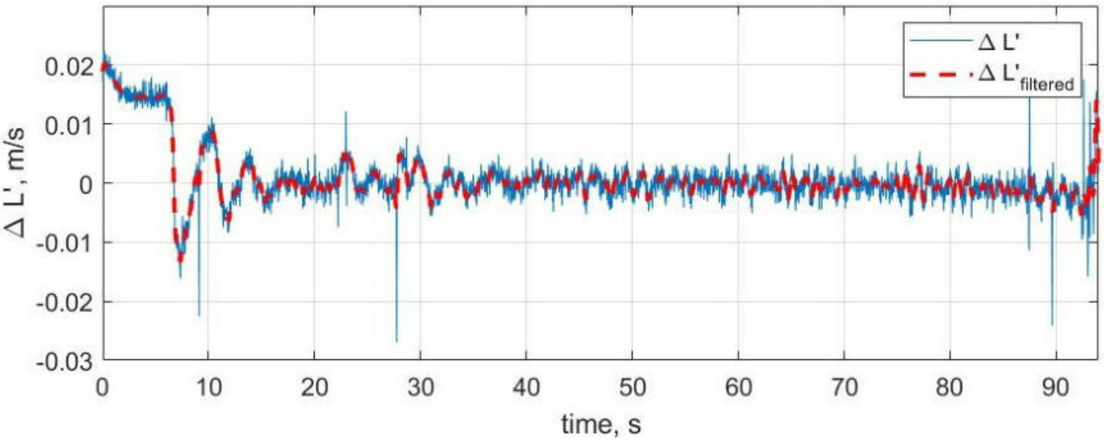

Figure 6.6: Speed deviation of the mockup from the imposed target profile as measured by the MC system. The speed signal has beed filtered with a cutoff frequency of $f_{cut} = 1$Hz.

provided by the tape tension. The tape is in fact tensioned by the joint action of the thrust and the tape rewinding, which due to the mockup inertia generates a force on the tape itself; if the body rotates, the arm joining the body center of gravity with the tape exit location is not parallel with the tape exerted force, thus generating a torque, named *restoring torque* since its action is always opposite to the body rotation and proportional to the angular displacement from the neutral condition.

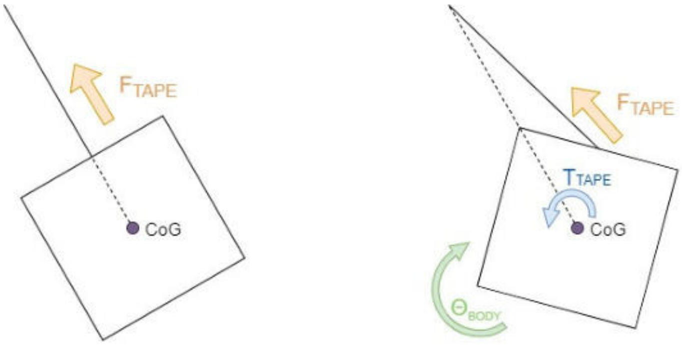

Figure 6.7: Schematization of the restoring torque due to tape tension and rotation of the mockup.

The restoring torque is present in the deployment scenario as well, with the difference being that the body is moving away from the post, therefore the tape tension - and consequently the restoring torque - is smaller.
Thanks to the tape exerted torque the trajectory shows a larger rotation radius, i.e. a more linear path has been followed.

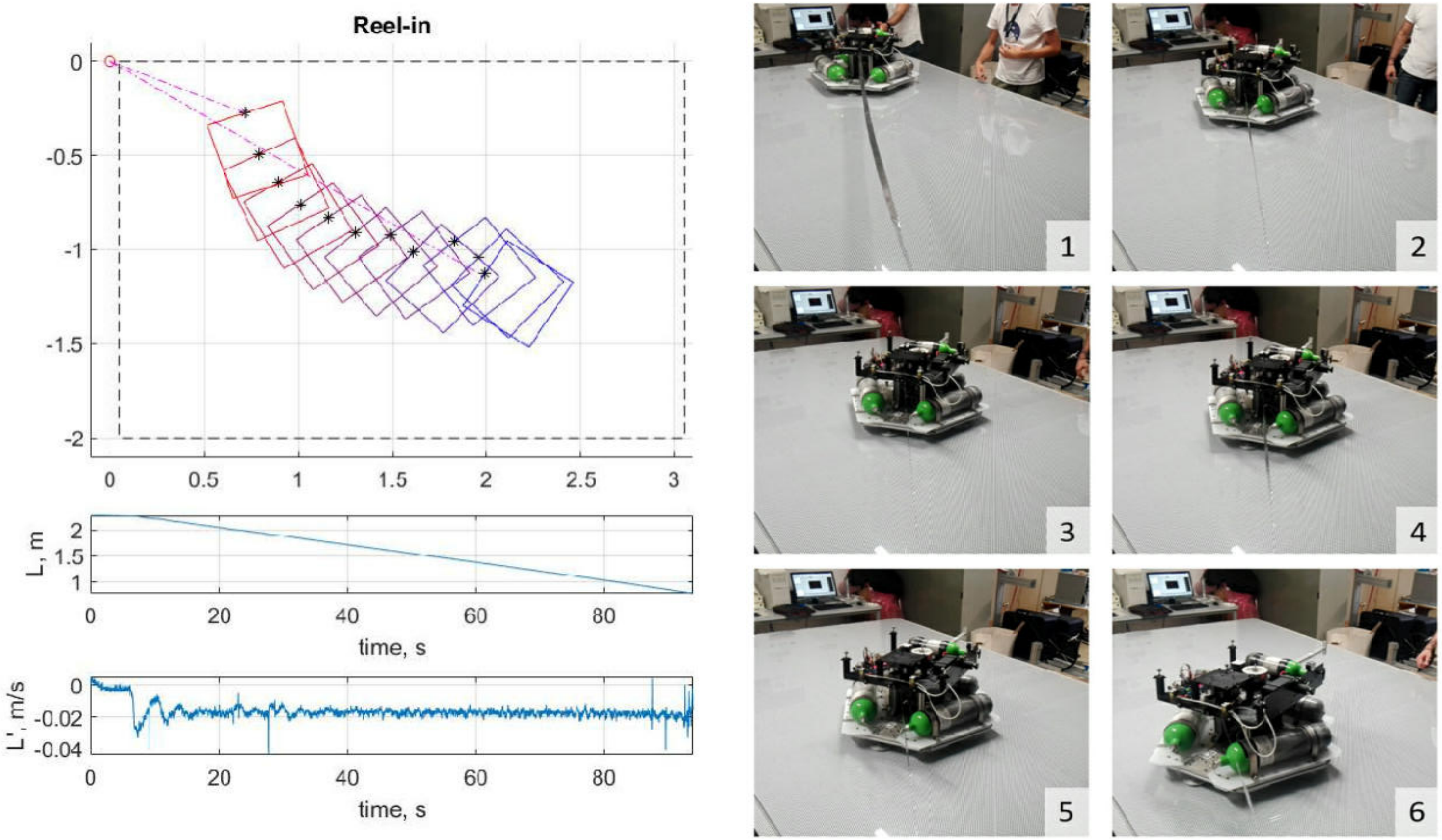

Figure 6.8: Mockup position reconstructed by MC data during reel-in manoeuver (left): 2D module position on the test table (top left), deployed length (middle left) and deployment rate (bottom left); comparison with frames captured from the test video (right).

Chapter 7

Conclusions

The work carried out by this thesis has aimed to design, develop, realize and test part of the mockup of an European technology demonstrator, whose task is to provide an accessible and effective way of deorbiting spent and decommissioned bodies - above all spacecrafts at end of life - from Low Earth Orbit (LEO) regions.

The mockup was conceived to replicate the original E.T.Pack system, thus involving a rotating wheel from which a thin tape-shaped tether is extracted and deployed in a controlled manner by means of a pulleys assembly, namely the PARCAE subsystem. Its design has involved researching the best hardware configuration to satisfy the given constraints, requiring compromises to be made between the ideal configuration and a feasible one: two motors were picked and sized, following a dynamic simulation of the system, to drive the main pulleys assembly and to brake the reel rotation, while still allowing for subsequent rewinding of the tape. A control and data handling subsystem has been conceived to cope with the hardware needs and the requirements of the experimental campaign, meant for remote control of the mockup, real time telemetry visualization and acquisition, multiple simultaneous control stations and future system expandability.

The whole system was planned in CAD and built in-house, often through the use of additive manufacturing techniques (FDM 3D printing) of PLA plastic. Electronics and control boards were assembled and soldered ad hoc as well.

Following functional tests at the component and subsystem level, the mockup was assembled in the final planned configuration and utilized for the first experimental campaign.

7.1 Achievements

The system performed as intended, producing valuable empirical data concerning both the mockup itself and the E.T.Pack deployment strategy under investigation. The major accomplishments for the two distinct cases are here briefly tackled.

Mockup

The mockup behavior was as expected, with no major issued to be highlighted. Startup, deployment, reel-in and thrust routines executed nominally during every preliminary or experimental test; telemetry transmission, acquisition and visualization was observed to be reliable, with very limited delay in dispatching commands and no losses of signal.

Tape mushing into the pulleys flanges was observed during the first reel-in demonstrations, and addressed with two additional 3D printed surfaces directing the tape correctly at the right position. Besides being this phenomenon a problem for the mockup, it gives useful insights for future mission planning: being the tape very unlikely in plane with the pulleys, additional guidance needs to be provided if rewinding - other than deployment - is desired.

Moreover, uncontrolled attitude during deployment was found, due to the rotation of the reel and conservation of angular momentum of the system. The issue was not solved during this first campaign but is planned to be addressed in the future.

E.T.Pack

Validation of the rotating reel design was performed, satisfying the prime goal of the work here presented. With the appropriate attitude control - which is already planned for the actual E.T.Pack system - deployment of a 25 mm wide aluminum tape from a rotating spool was proven to be achievable, and following a preset deployment profile feasible.

No issues with the tape being caught inside the pulleys flanges were noticed during deployment, thanks to a guiding, freely rotating pulley; issues during reel-in were on the contrary observed, and have already been cited.

A strong interaction between the thrusters ejecta and the deployed tape was also found, mostly in cases when the tape was not kept tense by the insufficient thrust. Ongoing investigations are studying the phenomenon.

Lastly, restoring torque due to the tape tension was observed. That is not an unforeseen behavior, since it was already accounted for during E.T.Pack design, but an empirical confirmation was here given.

7.2 Future developments

The work until here conducted is open to many further improvements, the main of which are as follows. As far as the physical mockup is concerned, technical upgrades are needed or desired: for the electronics, a definitive and more refined dedicated PCB could be designed, eliminating the need for jumper cables; further testing regarding DC motors and torque control via buck converters could be carried on, investigating open loop reel-in operations; attitude control, either via distinct thrusters firings or an independent actuator (e.g. reaction wheels) is needed to maintain a linear trajectory; closed loops for braking torque control - partially under current investigation - to reduce the load on the driver stepper and for accurate deployment.

Regarding the experimental work instead, more accurate deployment tests are foreseen, aiming at capturing the dynamic of the system and its responses to various external interactions, to fully characterize the behavior of the rotating reel system. Moreover, since reel-in operations have shown to be replicable with the mockup, further planning is being done in this regard as well.

Beyond the work for the E.T.Pack project, the mockup opens possibilities for demonstrative tug operations, non collaborative objects retrieval and rendez-vous manoeuver with proactive vehicles, providing testing abilities of tethered systems in a low friction environment.

Appendix A

Bare Electro-Dynamic Tether

Given a conductive tether of length L moving at relative speed $\vec{v}_{rel}$ in a magnetic field $\vec{B}$, an electromotive force E_{mf} is developed across its extremities and can be computed as

$$E_{mf} = \vec{v}_{rel} \times \vec{B} \cdot L$$

If electrons are emitted at the cathode and collected at the anode, thus establishing a current I, a force is generated on the tether, from Lorentz's law

$$\vec{F} = I\vec{L} \times \vec{B}$$

with the anode alternatively being:

- a tip electron collector, with the conductive tether surface isolated from the environment, resulting in a so called electro-dynamic tether;
- the whole uninsulated tether, resulting in a bare electro-dynamic tether.

Bare EDTs offer two big advantages over insulated ones, these being removing the need for an external bulky and heavy electrons collection surface and offering a more effective way - in terms of collected electrons per unit area - with respect to tip spheres, as the one used by the TSS-1R experiment [49, 50]

The generated force acting on the tape can be exploited to passively deorbit spent satellites by steadily lowering their perigee, or, alternatively, can be used to propel the spacecraft thus gaining altitude or varying orbital parameters. In the latter case current inversion is needed, achieved by inverting the E_{mf} polarity; therefore, an additional external power source to counteract the generated E_{mf} is needed.

EDT are only effective in presence of an external magnetic field, and their effectiveness varies with $\vec{B}$ modulus and the collected electrons count; good performances are achievable in LEO where the magnetic field $|B|$ is greater and the ionosphere is more dense, whilst loosing efficiency in higher orbits.

Appendix B

Testbed Code Base

The whole codebase for the microcontrollers running and controlling both the testbed and the ancillary sensors must be well structured and organized to allow for easy maintenance and bug tracing; moreover, expandability is paramount in this stage of the projects, as other modules and extensions are likely to be added to enhance the mockup potential. At the time of writing, an additional Arduino UNO is being planned to be added in continuation of the work herein described to perform attitude control and determination; its addition has been facilitated by the usage of I2C and a modular code.

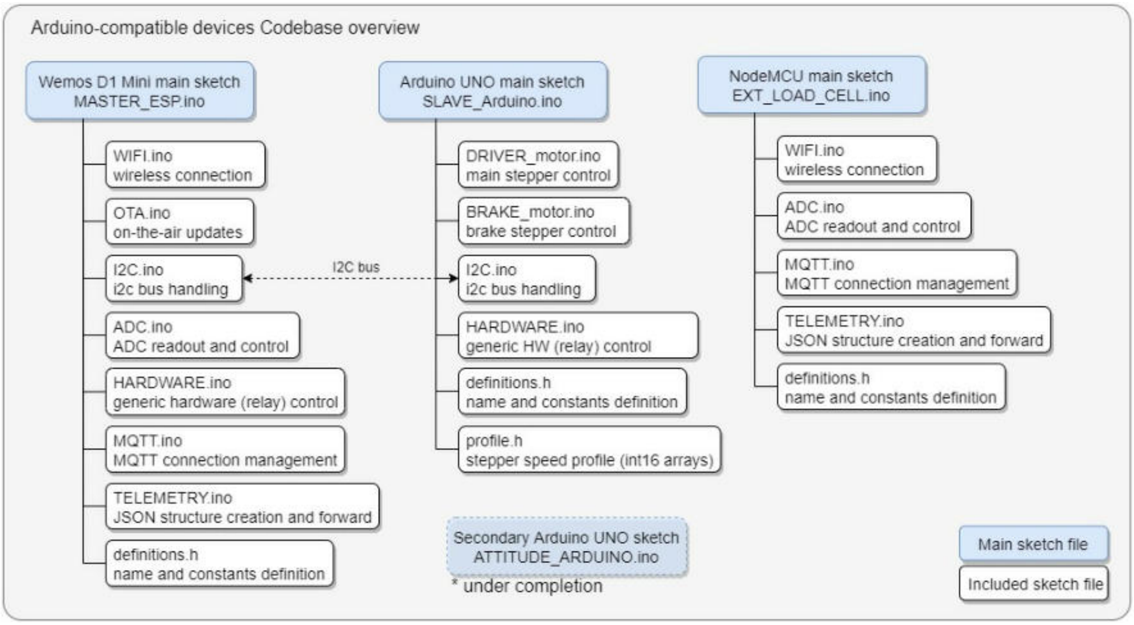

Figure B.1: Codebase structure for the microcontrollers code.

Furthermore, collaboration is another key point of this effort, as the project will be overtaken by other students in the next future.

With this in mind, the codebase has been structured by topic and functionality, gathering functions performing tasks of the same functional area in files, to then include them in the main Arduino document. Functions and callback have been thoroughly commented to describe their task and relationship with others.

The Arduino core codebase organization and structure is briefly documented in Figure B.1.

The MATLAB source code and runtime file for the control station has been uploaded to the shared repository as well; however, being the MATLAB *.mlapp* extension a proprietary, non-text encoded filetype, only marginal revision tracing is feasible, lacking the ability of per-codeline git control and versioning.

The resulting corpus of Arduino and MATLAB code, documentation, procedures and components datasheets have been uploaded to a GitHub repository; in this way collaboration and modification tracking is feasible, enabling all participants to remain up-to-date with the latest code revision. Versioning is in this context an useful feature, allowing to trace modifications and revert back to the latest stable version in case of a disruptive change.

Bibliography

[1] M. Kruijff, "Yes2 inherently-safe tethered re-entry mission and contingencies," in *54th International Astronautical Congress of the International Astronautical Federation, the International Academy of Astronautics, and the International Institute of Space Law*, pp. IAA–6, 2003.

[2] "ESA MASTER Statistics." `https://sdup.esoc.esa.int/discosweb/statistics/`. Accessed: 21/03/2020.

[3] "USSPACECOM Space Track Website." `https://space-track.org/#boxscore`. Accessed: 20/03/2020.

[4] "ESA MASTER Website." `https://sdup.esoc.esa.int/`, (accessed June 12, 2020).

[5] "NASA LEGEND Website." `https://www.orbitaldebris.jsc.nasa.gov/modeling/legend.html`, (accessed June 12, 2020).

[6] J. C. McDowell, "The low earth orbit satellite population and impacts of the spacex starlink constellation," *The Astrophysical Journal Letters*, vol. 892, no. 2, p. L36, 2020.

[7] R. H. Freeman, "Overview: Satellite constellations," *Journal of Space Operations & Communicator (ISSN 2410-0005)*, vol. 17, no. 2, 2020.

[8] National Research Council, *Orbital Debris: A Technical Assessment.* Washington, DC: The National Academies Press, 1995.

[9] D. J. Kessler, N. L. Johnson, J. Liou, and M. Matney, "The kessler syndrome: implications to future space operations," *Advances in the Astronautical Sciences*, vol. 137, no. 8, 2010.

[10] D. J. Kessler and B. G. Cour-Palais, "Collision frequency of artificial satellites: The creation of a debris belt," *Journal of Geophysical Research: Space Physics*, vol. 83, no. A6, pp. 2637–2646, 1978.

[11] UNOOSA Scientific and Technical Subcommittee, "Space Debris Mitigation Guidelines of the Committee on the Peaceful Uses of Outer Space," 2010. A/AC.105/890.

[12] ASI, BNSC, CNES, DLR, ESA, "European Code of Conduct for Space Debris Mitigation." `http://unoosa.org/documents/pdf/spacelaw/sd/2004-B5-10.pdf`, 2006, accessed April 3, 2020.

[13] ASI, CNES, CNSA, CSA, DLR, ESA, ISRO, JAXA, KARI, NASA, ROSCOSMOS, SSAU, UKSA, "IADC Space Debris Mitigation Guidelines," Sept. 2007. IADC-02-01, Rev. 1.

[14] R. Janovsky, "End-of-life de-orbiting strategies for satellites," in *54th International Astronautical Congress of the International Astronautical Federation, the International Academy of Astronautics, and the International Institute of Space Law*, pp. IAA–5, 2002.

[15] G. Sánchez-Arriaga, J. Sanmartín, and E. C. Lorenzini, "Comparison of technologies for deorbiting spacecraft from low-earth-orbit at end of mission," *Acta Astronautica*, vol. 138, pp. 536–542, 2017.

[16] G. Sánchez-Arriaga, S. Naghdi, K. Wätzig, J. Schilm, E. Lorenzini, M. Tajmar, E. Urgoiti, L. T. Castellani, J. Plaza, and A. Post, "The et pack project: Towards a fully passive and consumable-less deorbit kit based on low-work-function tether technology," *Acta Astronautica*, 2020.

[17] A. Francesconi, C. Giacomuzzo, F. Branz, and E. Lorenzini, "Survivability to hypervelocity impacts of electrodynamic tape tethers for deorbiting spacecraft in leo," in *6th European Conference on Space Debris*, pp. 22–25, European Space Operations Centre Darmstadt, Germany, 2013.

[18] A. Valmorbida, M. Mazzucato, S. Tronco, S. Debei, and E. C. Lorenzini, "Spartans-a cooperating spacecraft testbed for autonomous proximity operations experiments," in *2015 IEEE International Instrumentation and Measurement Technology Conference (I2MTC) Proceedings*, pp. 739–744, IEEE, 2015.

[19] A. Valmorbida, M. Mazzucato, and M. Pertile, "Calibration procedures of a vision-based system for relative motion estimation between satellites flying in proximity," *Measurement*, vol. 151, p. 107161, 2020.

[20] A. Valmorbida, M. Mazzucato, S. Tronco, M. Pertile, and E. Lorenzini, "Design of a ground-based facility to reproduce satellite relative motions," in *2017*

IEEE International Workshop on Metrology for AeroSpace (MetroAeroSpace), pp. 468–473, IEEE, 2017.

[21] E. Lungavia Master's thesis, Università degli Studi di Padova, Italy. In pubblication (2021).

[22] R. Mantellato, L. Olivieri, and E. Lorenzini, "Study of dynamical stability of tethered systems during space tug maneuvers," *Acta Astronautica*, vol. 138, pp. 559–569, 2017.

[23] V. Aslanov and V. Yudintsev, "Dynamics of large space debris removal using tethered space tug," *Acta Astronautica*, vol. 91, pp. 149–156, 2013.

[24] L. Olivieri, F. Sansone, M. Duzzi, and A. Francesconi, "Ted project: Conjugating technology development and educational activities," *Aerospace*, vol. 6, no. 6, p. 73, 2019.

[25] M. J. Mashayekhi and A. K. Misra, "Optimization of tether-assisted asteroid deflection," *Journal of Guidance, Control, and Dynamics*, vol. 37, no. 3, pp. 898–906, 2014.

[26] S.-J. Chung, D. Adams, A. Saenz-Otero, E. Kong, D. W. Miller, D. Leisawitz, E. Lorenzini, and S. Sell, "Spheres tethered formation flight testbed: advancements in enabling nasa's specs mission," in *Advances in Stellar Interferometry*, vol. 6268, p. 62680B, International Society for Optics and Photonics, 2006.

[27] G. Sarego, L. Olivieri, A. Valmorbida, A. Brunello, E. C. Lorenzini, L. Tarabini Castellani, E. Urgoiti, A. Ortega, G. Borderes-Motta, and G. Sánchez-Arriaga, "Deployment requirements for deorbiting electrodynamic tether technology," AEC 2020, Bordeaux, 2020.

[28] L. N. Egidio, H. R. Daiha, G. S. Deaecto, and J. C. Geromel, "Dc motor speed control via buck-boost converter through a state dependent limited frequency switching rule," in *2017 IEEE 56th Annual Conference on Decision and Control (CDC)*, pp. 2072–2077, IEEE, 2017.

[29] D. Offner and N. Tomita, "Determining the coefficient of friction for rolling disks," 1978.

[30] V. Deltoro, *Electric Machines and Power Systems.* Prentice-Hall, 1985.

[31] G. Baluta, "Microstepping mode for stepper motor control," in *2007 International Symposium on Signals, Circuits and Systems*, vol. 2, pp. 1–4, IEEE, 2007.

[32] M. Bodson, J. N. Chiasson, R. T. Novotnak, and R. B. Rekowski, "High-performance nonlinear feedback control of a permanent magnet stepper motor," *IEEE Transactions on Control Systems Technology*, vol. 1, no. 1, pp. 5–14, 1993.

[33] "ACE FDT-47 Datasheet." `https://docs.rs-online.com/03a1/0900766b8146f804.pdf`, (accessed April 10, 2020).

[34] S. Lennert and M. P. Cartmell, "Analysis and design of a friction brake for momentum exchange propulsion tethers," *Acta Astronautica*, vol. 59, no. 8-11, pp. 923–930, 2006.

[35] X. Nian, F. Peng, and H. Zhang, "Regenerative braking system of electric vehicle driven by brushless dc motor," *IEEE Transactions on Industrial Electronics*, vol. 61, no. 10, pp. 5798–5808, 2014.

[36] J. Zhang, S. Li, G. Lu, and Q. Zhou, "A novel regenerative braking method of bldcm for wheeled mobile robot," in *The 2010 IEEE International Conference on Information and Automation*, pp. 676–681, IEEE, 2010.

[37] C. Gökçe, Ö. Üstün, and A. Y. Yeksan, "Dynamics and limits of electrical braking," in *2013 8th International Conference on Electrical and Electronics Engineering (ELECO)*, pp. 268–272, IEEE, 2013.

[38] X. Zhou and J. Fang, "Precise braking torque control for attitude control flywheel with small inductance brushless dc motor," *IEEE Transactions on Power Electronics*, vol. 28, no. 11, pp. 5380–5390, 2013.

[39] W. P. R. Ned Mohan, Tore M. Undeland, *Power Electronics: Converters, Applications,and Design*, ch. 7, pp. 174–178. John Wiley and Sons, 2003.

[40] L. Xheladini, A. Polat, and L. Ergene, "Design of high frequency buck converter for dc motor control," in *2015 Intl Aegean Conference on Electrical Machines & Power Electronics (ACEMP), 2015 Intl Conference on Optimization of Electrical & Electronic Equipment (OPTIM) & 2015 Intl Symposium on Advanced Electromechanical Motion Systems (ELECTROMOTION)*, pp. 768–773, IEEE, 2015.

[41] J. U. Agber, "Analysis of detent torque in hybrid stepping motors," *International Journal of Engineering and Science (IJES)*, vol. 2, no. 5, pp. 35–41, 2013.

[42] R. H. Brown and M. Jaroudi, "Torque prediction and maximization strategies for bifilar-wound hybrid step motors," *IEEE transactions on power electronics*, vol. 7, no. 3, pp. 535–541, 1992.

[43] NXP Semiconductors, *UM10204: I2C-bus specification and user manual*, 2014 (accessed July 27, 2020).

[44] "Arduino stepper library." `https://github.com/arduino-libraries/Stepper`, (accessed April 17, 2020).

[45] "Accelstepper arduino library." `http://www.airspayce.com/mikem/arduino/AccelStepper`, (accessed April 16, 2020).

[46] "MQTT Website." `http://mqtt.org/`, (accessed July 16, 2020).

[47] "OpenWRT Website." `https://openwrt.org/`, (accessed July 28, 2020).

[48] L. Olivieri, A. Valmorbida, G. Sarego, E. Lungavia, D. Vertuani, and E. C. Lorenzini, "Test of tethered deorbiting of space debris," 2020.

[49] M. Dobrowolny and N. Stone, "A technical overview of TSS-1: the first tethered-satellite system mission," *Il Nuovo Cimento C*, vol. 17, no. 1, pp. 1–12, 1994.

[50] R. D. Estes, E. Lorenzini, J. Sanmartin, J. Pelaez, M. Martinez-Sanchez, C. Johnson, and I. Vas, "Bare tethers for electrodynamic spacecraft propulsion," *Journal of Spacecraft and Rockets*, vol. 37, no. 2, pp. 205–211, 2000.